

## Autonomous Tuning and Charge-State Detection of Gate-Defined Quantum Dots

J. Darulová<sup>1,\*</sup>, S.J. Pauka,<sup>2</sup> N. Wiebe,<sup>3,4</sup> K.W. Chan<sup>5</sup>, G.C. Gardener,<sup>6,7</sup> M.J. Manfra,<sup>6,7,8,9</sup>  
M.C. Cassidy<sup>5</sup> and M. Troyer<sup>10</sup>

<sup>1</sup> *Theoretische Physik, ETH Zurich, 8093 Zurich, Switzerland*

<sup>2</sup> *ARC Centre of Excellence for Engineered Quantum Systems, School of Physics, The University of Sydney, Sydney, NSW 2006, Australia*

<sup>3</sup> *Pacific Northwest National Laboratory, Richland, Washington 99354, USA*

<sup>4</sup> *Department of Physics, University of Washington, Seattle, Washington 98195, USA*

<sup>5</sup> *Microsoft Quantum, The University of Sydney, Sydney, NSW 2006, Australia*

<sup>6</sup> *Birck Nanotechnology Center, Purdue University, West Lafayette, Indiana 47907, USA*

<sup>7</sup> *Microsoft Quantum Purdue, Purdue University, West Lafayette, Indiana 47907, USA*

<sup>8</sup> *Department of Physics and Astronomy, Purdue University, West Lafayette, Indiana 47907, USA*

<sup>9</sup> *School of Materials Engineering and School of Electrical and Computer Engineering, Purdue University, West Lafayette, Indiana 47907, USA*

<sup>10</sup> *Microsoft Quantum, Redmond, Washington 98052, USA*

(Received 27 November 2019; revised manuscript received 27 January 2020; accepted 13 April 2020; published 4 May 2020)

Defining quantum dots in semiconductor-based heterostructures is an essential step in initializing solid-state qubits. With growing device complexity and increasing number of functional devices required for measurements, a manual approach to finding suitable gate voltages to confine electrons electrostatically is impractical. Here, we implement a two-stage device characterization and dot-tuning process, which first determines whether devices are functional and then attempts to tune the functional devices to the single or double quantum-dot regime. We show that automating well-established manual-tuning procedures and replacing the experimenter's decisions by supervised machine learning is sufficient to tune double quantum dots in multiple devices without premeasured input or manual intervention. The quality of measurement results and charge states are assessed by four binary classifiers trained with experimental data, reflecting real device behavior. We compare and optimize eight models and different data preprocessing techniques for each of the classifiers to achieve reliable autonomous tuning, an essential step towards scalable quantum systems in quantum-dot-based qubit architectures.

DOI: 10.1103/PhysRevApplied.13.054005

### I. INTRODUCTION

Quantum computers are expected to solve a range of problems intractable for classical computers, such as factoring of large integers [1], simulating quantum systems [2–5], and efficiently sampling correlated probability distributions [6,7]. Useful quantum computers with millions of high-quality qubits are still some way off, but early prototypes with 50–100 qubits, referred to as noisy intermediate-scale quantum (NISQ) systems, are already available [6,8,9]. For these NISQ systems, accuracy and reliability of quantum-gate operations, and hence qubit quality, are essential. Even before qubits can be used to execute quantum algorithms, large-scale material and design studies are necessary to optimize fabrication and device yield, involving both characterization and initial

qubit tuning. Given the success of machine learning (ML) and artificial intelligence (AI) in recent years, it is worth investigating their capabilities in solid-state qubit measurements.

Electrostatically defined quantum dots are the building blocks for a range of solid-state qubit architectures based on charge [10–12], spin [13–16], and topologically protected states [17–19]. Fabrication variances as well as defects within the material lead to a disordered background potential landscape, which must be compensated for by different gate voltages when defining quantum dots. As this disorder is random, each gate within each device has a unique optimal voltage, which must be set and updated over time. This tuning step is an essential, yet repetitive task well suited to automation. The increasing complexity as the number of qubits per chip grows has motivated several approaches to partially automate key components of this process. Neural networks have been successfully

\* djana@itp.phys.ethz.ch

used to detect charge states on nearly noiseless data [20–22] and procedures to automate fine tuning of the interdot tunnel coupling [23–26] as well as the fitting of charge transitions in charge-stability diagrams [27] have been implemented. Together with studies improving measurement efficiency [28,29], implementing the tune up of a known device [30], and automating the search for a single-electron regime [31,32], these results are stepping stones for automated tuning of electrostatically defined quantum dots. They have been, however, demonstrated on single, pretuned devices requiring ideal measurement results and significant manual input such as promising voltage ranges or decisions whether the desired regime has been found. Autonomous tuning of unknown devices is a key milestone required for applying these techniques to practical tuning situations.

Here we demonstrate a device characterization and tuning sequence on multiple devices without premeasured input and manual intervention. We implement a so-called minimal viable product, a standard software-development technique in which a product is developed with sufficient features to satisfy early users and initiate a feedback loop to guide future improvements. Based on the QCoDes PYTHON control software [33], we develop a software package, tuning semiconductor qubit devices into a double-dot regime. We only require the devices' gate layout, bonding scheme, line mappings, safe gate-voltage ranges, and the setup-specific noise floor as input. Using gate-defined quantum dots in GaAs as a proxy qubit device, we demonstrate that our software is capable of tuning different devices at different locations within the same wafer over two cooldowns.

## II. TUNING APPROACH

Quantum dots are systems confining electrons or holes in regions small enough to make their quantum mechanical energy levels observable. To form gate-defined quantum dots in GaAs, lithographically fabricated gate electrodes on the surface of the GaAs/Al<sub>0.3</sub>Ga<sub>0.7</sub>As heterostructure are used to deplete a 2DEG beneath them, forming isolated puddles of charges with a physical dimension on the order of the Fermi wavelength [34].

Manual tuning of gate-defined quantum dots involves a series of 1D and 2D measurements, measuring current through the device as a function of one or two gate voltages respectively, and utilizes informed guesses and the intuition of the experimenter. These measurements narrow down the large parameter space to find a voltage combination defining the desired quantum-dot structure. Material defects, impurities, fabrication variations, capacitive couplings between gates and hysteresis make these voltages unique to each device and difficult to find. Automation of these procedures will remove a manual, time-consuming task and enable many devices to be tuned in parallel, which

is an important element for a large-scale quantum processor. To fully benefit from such a progress, automated procedures need to be fully independent and not rely on premeasured input or manual intervention.

Given the success across a variety of fields, machine-learning techniques are promising tools to use. Machine learning is commonly considered for two types of problems. First, it is used to solve problems too complex for predefined, structured programs such as face recognition [35], speech-to-text processing [36], and spam filtering [37]. Our lack of understanding of good algorithms to perform these tasks makes them natural candidates for machine learning. Second, it can be used to improve solutions even where good classical algorithms are already known, as for example the simulation of quantum many-body systems [38–40] as well as designing methods for encoding and decoding quantum information within error-correcting codes [41,42].

As quantum-dot tuning is routinely performed by scientists and quantum dots have been studied extensively in the past [34], we choose an approach, which automates existing procedures with simple machine-learning tools to achieve autonomous quantum-dot tuning. Specifically, we implement a deterministic tuning sequence and replace the scientists' knowledge by binary classifiers trained on experimental data. We use approximately 10 000 hand-labelled datasets to ensure that features difficult to simulate, such as realistic noise and poor or intermediate dot regimes, are learned. By automating 1D and 2D measurements and their respective data analysis (see Sec. IV A and IV B), and using four binary classifiers available in Python's scikit-learn, Sec. IV C, we are able to characterize and tune several devices with no premeasured input. Fig. 1 illustrates this strategy. First, a gate leakage test identifies shorted gates and an initial quality assessment preselects devices featuring a current above the setup-specific noise floor. Next, we use 1D measurements to characterize all gates of all devices available, as described in Sec. V. Using a binary classifier we predict the quality of each measurement and establish a list of working gates of each device. If all gates respond well, the device is selected for tuning. The tuning algorithm uses a sequence of 1D measurements to narrow down and set voltages and a 2D measurement classified by three binary classifiers to assess the dot regime, see Sec. VI. We show that a predefined sequence of fast 1D and a few 2D measurements together with binary classifiers is sufficient to reach the desired regime and that no complex machine-learning algorithms are required to perform this well-studied task.

## III. DEVICES

We use double quantum dots formed in a GaAs/Al<sub>0.3</sub>Ga<sub>0.7</sub>As 2DEG depleted by the gate structure illustrated in Fig. 2(a) [43] as an example system to

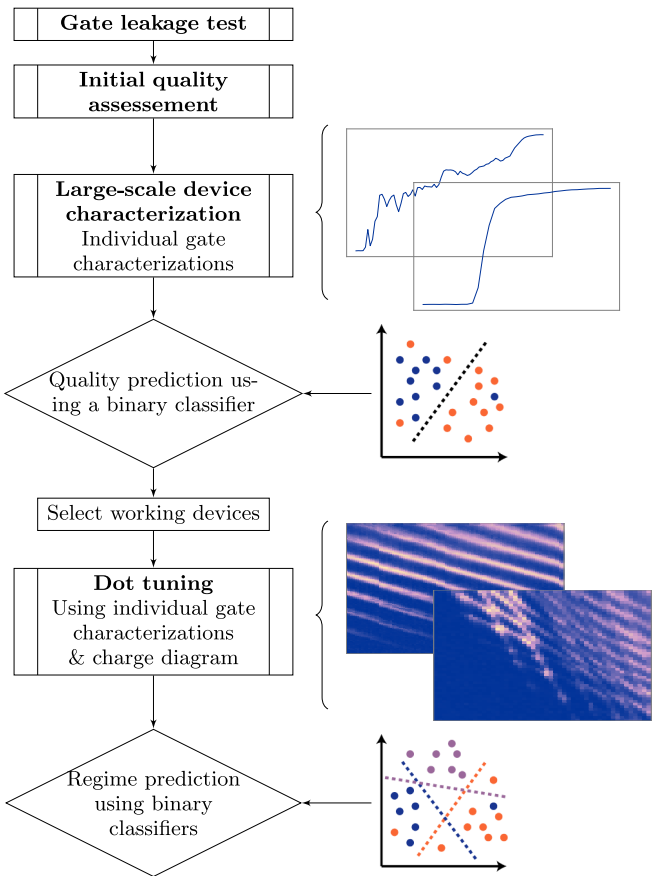


FIG. 1. Workflow of characterizing and tuning an unknown device. First, all gates are tested for leakage, detecting possible connections shorting gates together. Then, in an initial basic quality assessment, we determine if any current is flowing through the device. We then individually characterize all gates of the device through one-dimensional (1D) measurements. The quality of the gate response is assessed using a binary classifier and all gate responses need to be classified as good for a device to be selected for tuning. With the initial gate quality assessment and device characterization we are able to distinguish two types of failure: no current through the device, or unresponsive gates. The tuning algorithm is a sequence of 1D measurements reducing the relevant voltage space and one or more two-dimensional (2D) measurements establishing a charge-stability diagram. Charge state and quality are established by a combination of three binary classifiers.

demonstrate the performance of our autonomous tuning package. This system of gates and dots can be approximated classically by a network of tunneling resistances and capacitors, called the constant interaction model [34], illustrated in Fig. 2(b).

The 2DEG is located 91 nm below the surface of the GaAs/Al<sub>0.3</sub>Ga<sub>0.7</sub>As heterostructure of density  $1.5 \times 10^{11} \text{ cm}^{-2}$  and mobility  $2.4 \times 10^6 \text{ cm}^2/\text{V s}$ . An aluminum oxide layer deposited using atomic layer deposition separates TiAu gates from the heterostructure and enables positive voltages to be applied without gate leakage. Our

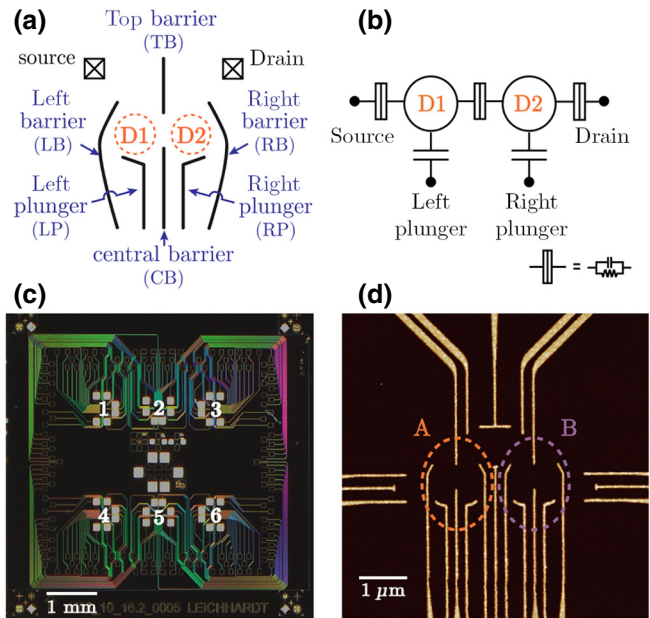


FIG. 2. (a) Gate arrangement of a device. Six metallic gates are used to deplete the 2DEG underneath. Barrier gates create potential wells confining electrons within the 2DEG structure while plunger gates vary the electrochemical potential of the dots. Current through the device is measured between source and drain. (b) Simplified capacitance model representing a double quantum dot. The two dots are coupled to source, drain, and two gates, while barriers are characterized by tunnel resistors and a capacitor. (c) Optical micrograph of a chip containing six device pairs, a prototype for future scalable quantum processor. It consists of 132 dc lines connected to metallic gates, for each of which a valid voltage needs to be determined. (d) False-color scanning electron micrograph showing the active region of one of the device pairs. It can host up to five dots, where two double dots (A and B) are used as qubits, potentially coupled via a single dot located between them [44]. We tune one double dot at a time.

test chip, which holds six pairs of double quantum dots on a  $5 \times 5 \text{ mm}^2$  chip, is displayed in Fig. 2(c) and a false-color scanning electron micrograph of one device pair in Fig. 2(d). It allows us to study multiple double quantum dots formed in a single fabrication run, while reducing variations caused by fabrication. We bonded four of the six available device pairs, located in the corners of the chip and numbered 1, 3, 4, and 6.

The device layout, illustrated in Fig. 2(a), consists of two types of gates: barriers and plungers. The left barrier (LB), right barrier (RB), and central barrier (CB) create potential wells, defining tunnel resistances between quantum dots and reservoirs. Left plunger (LP) and right plunger (RP) tune the electrochemical potential and are used to change the number of electrons in a quantum dot. These six gates constitute what is called a *device*. All voltages applied to these gates need to lie within a known safety range [ $V_i^{\text{safe min}}, V_i^{\text{safe max}}$ ], protecting against dielectric breakdown.

The purpose of tuning is to determine gate voltages leading to one of two well-defined states with either a single or two separate quantum dots formed, referred to as single- and double-dot regimes.

Devices A and B of each device pair on the chip are tuned separately. Experiments are performed in a dilution refrigerator with a base temperature of 20 mK and at zero magnetic field. All measurements are direct transport measurements using standard lock-in techniques.

#### IV. METHODS

The device characterization and dot-tuning algorithms are implemented by a modular software consisting of two main modules, each representing an essential manual tuning step: a 1D, single gate characterization and a 2D measurement generating a charge-stability diagram. These modules take and analyze data for tuning and preprocess it for machine-learning classification. Outcomes are classified using binary classifiers, assessing quality, and, in case of charge-stability diagrams, charge regime. The classification outcomes determine next actions to take, such as whether a device will be tuned after characterization or which gate voltage to adjust during tuning.

At the beginning of each run we determine the saturation current  $A_{\max}$  with all  $V_i = 0$ , which is used to normalize data before classification. If  $A_{\max}$  is below the setup-specific noise level, the device is declared not working and not considered for characterization or tuning.

##### A. Individual gate characterization

The individual gate characterization module determines the voltage range in which a gate partially depletes the underlying 2DEG for a given device configuration. This is the interesting voltage range for further tuning. The voltage  $v$  of the gate in question is varied while keeping all other gates constant. The measured  $I$ - $V$  curve, also called pinch-off curve, is normalized by  $A_{\max}$  and smoothed using Gaussian kernel convolution. The curve is then fitted to

$$f(x, a, b, c) = a[1 + \tanh(bx + c)], \quad (1)$$

extracting amplitude  $a$ , slope  $b$ , and offset  $c$ . Here,  $x$  is the normalized gate voltage

$$x = \frac{v - v_{\min}}{v_{\max} - v_{\min}}, \quad (2)$$

where  $v_{\min}$  and  $v_{\max}$  are the highest and lowest voltage setpoints, respectively. Similar to conventional semiconductor transistors, we are interested in gate voltages separating cutoff, transition and saturation regions  $V_i^L, V_i^H$ , see Fig. 3(a). Using methods described in Ref. [45], we define  $V_i^T$  as the point of highest variance of the measured current,

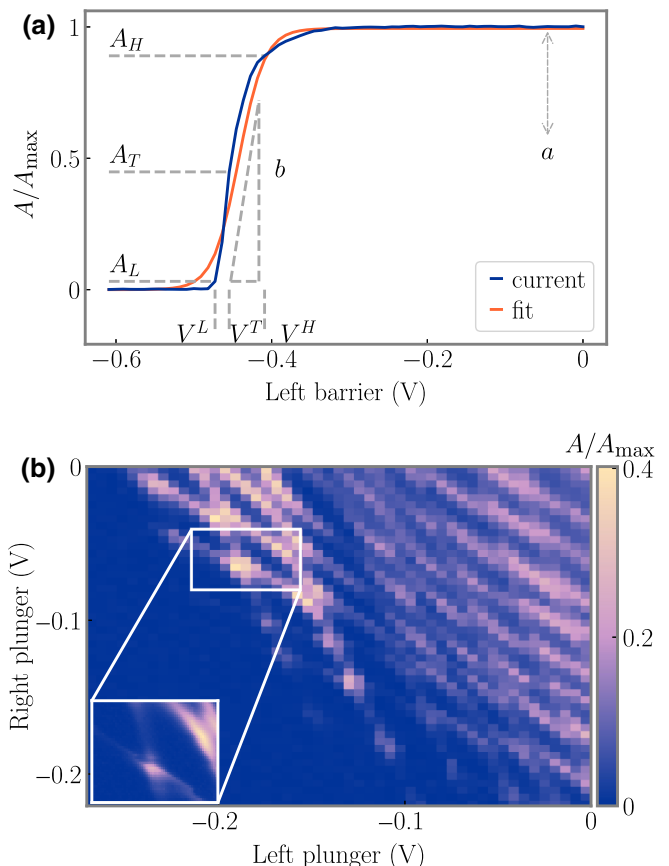


FIG. 3. (a) Data analysis of an individual gate characterization. A gate is stepped from high to low voltage safety limits until the signal falls below noise level. The fitting procedure extracts relevant features for classification, such as amplitude, slope, offset as well as relevant voltages for subsequent tuning  $V_i^L, V_i^T, V_i^H$ . These voltages are used to determine a suitable voltage to set or range to sweep. (b) Charge-stability diagram of a good double-dot regime. Two gates, typically plungers, are stepped within their valid ranges  $[V_i^L, V_i^H]$  to measure a 2D map. The result is segmented into  $0.05V \times 0.05V$  regions, which are classified individually to determine their quality and charge state.

the lower bound of the transition region  $V^L$  as the voltage axis intercept of the tangent at  $V_i^T$  and the upper bound  $V_i^H$  as the minimum of the second-order derivative of the current. Further tuning will continue by considering the range  $[V_i^L, V_i^H]$ .

Following standard machine-learning procedures, we select a set of features representing the measurement, also known as feature selection. Similar to a transistor, we are looking for a noiseless, sharp transition between fully open and fully closed regimes. The features extracted during fitting are amplitude, slope, offset, low current, high current, residuals, offset, and transition current. Voltages such as the transition voltage are not considered at this stage, as we do not optimize for transition locations in voltage space. By training and testing classifiers with all possible

subsets of features we find that the following ones are most relevant:

- (1) amplitude  $a$ ;
- (2) slope  $b$ ;
- (3) residuals;
- (4) pinch-off current  $A_L$ .

We thus use these to define the feature vector for pinch-off classification. Exposing a classifier to more than these parameters results in lower accuracy due to overfitting. We can, however, replace amplitude by high and low current or low current by offset.

## B. Charge-stability diagram

Charge-stability diagrams are measured by varying left and right plunger voltages over the voltage range  $[V_i^L, V_i^H]$ , changing electrochemical potentials of nearby dots while measuring current through the device. The purpose is to find regions in voltage space where single and double dots are formed. While gates could be swept in any order, we are stepping over the left plunger's range on the  $x$  axis and the right plunger's range on the  $y$  axis. The voltage ranges are sampled over 50 equidistant points. The number of setpoints is increased if the step size is larger than a threshold  $\delta V$ , which is smaller than both a device-specific safe-voltage step and a desired voltage resolution. As a compromise between measurement time and voltage resolution we choose  $\delta V < 0.005V$ . The resulting diagram is transformed using skimage's resize method [46]. Based on previously measured data we know that averages of currents in good quantum-dot regimes are within  $[0.004A_{\max}, 0.1A_{\max}]$ . We compare the average  $\bar{A}$  of each of the image's boundaries to these limits and update the plunger's current-voltage ranges according to the following rules:

- (1) if  $\bar{A}_{\text{left vertical}} > 0.1A_{\max}$ , decrease  $V_{LP}^L, V_{LP}^H$ ;
- (2) if  $\bar{A}_{\text{bottom horizontal}} > 0.1A_{\max}$ , decrease  $V_{RP}^L, V_{RP}^H$ ;
- (3) if  $\bar{A}_{\text{right vertical}} < 0.004A_{\max}$ , increase  $V_{LP}^L, V_{LP}^H$ ;
- (4) if  $\bar{A}_{\text{top horizontal}} < 0.004A_{\max}$ , increase  $V_{RP}^L, V_{RP}^H$ .

The measurement result is segmented into  $0.05V \times 0.05V$  regions, each of which is classified individually. We use three binary classifiers to assess quality and regime, trained to predict either single-dot quality, double-dot quality, and dot regime, respectively (see Sec. IV C for details). The module returns the success of measuring a charge diagram with respect to signal strength and quality as well as regime predictions of each segment. Our attempts in defining suitable features to represent charge-stability diagrams failed due to noise and large variability of the data. We thus use the full current map for classification.

## C. Classification

The task of supervised machine learning is to approximate an unknown target function  $f$

$$Y = f(X), \quad (3)$$

mapping input variables  $X$  to output variables  $Y$ . In the present dot-tuning algorithm,  $X$  is either postprocessed data or a smaller feature vector extracted from it, while  $f$  the mapping onto either quality (good or bad) or regime (single or double dot), as summarized in Table I. After labelling existing data, i.e., attaching a label  $Y$  to each  $X$ , we can train a machine-learning model to learn an approximation  $m$  of the unknown mapping function  $f$  and use it to predict labels of new measurements. In order to find an approximation, assumptions about its form need to be made. Different classifiers implement different types of functions  $m(X, h)$  with hyper parameters  $h$ . The task is to find an accurate model  $m$  and good hyper parameters  $h$ . A good model will not only accurately fit known  $X$  and  $Y$  relations, but also generalize well to new, previously unseen data. The more complex a model is, the more flexible it is to learn concepts of  $X$  and the more data it needs for training to avoid overfitting, a situation when noise and random fluctuations are learned as concepts.

The large variety of noise and intermediate regimes of quantum-dot measurements make it difficult to generate synthetic data reflecting real device behavior. For this reason, we use experimental data for training. We collect and label 4000 pinch-off curves, 4000 single-dot and 2500 double-dot current maps. Examples of good and bad results for each category are shown in Fig. 4. Data used for classifier training originate from three double-dot devices fabricated on two different chips and of the same architecture design as characterized and tuned here.

As the size of our training set is not large enough for algorithms containing many free parameters such as deep neural nets, we investigate the potential of simpler models that are easy to train and optimize. We compare classifiers

TABLE I. Summary of input  $X$  and output  $Y$  for each classifier used. Features extracted during individual gate characterizations (amplitude, slope, residuals, pinch-off current) form the 1D input vector to the pinch-off classifier. The output predicts the quality of the gate's response. Single-, double-, and dot-regime classifiers use the normalized current and its Fourier transform (FT) or both combined to predict qualities and regime, respectively. The outcomes of these classifiers guide the dot-tuning algorithm illustrated in Sec. VI.

Classifier	$X$	$Y$
Pinch off	Features	Good or bad
Single dot	Current data	Good or bad
Double dot	Current data	Good or bad
Dot regime	Current data	Single or double

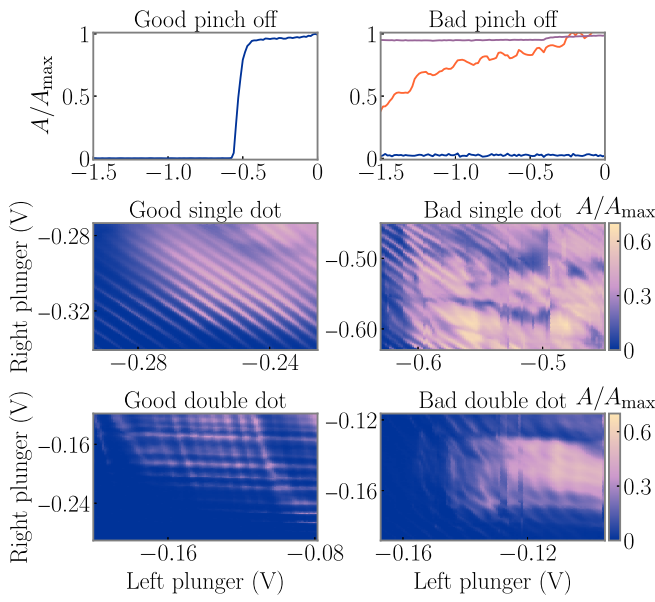


FIG. 4. Examples of data used for classification, showing normalized current  $A/A_{\max}$  as a function of one or two gate voltages. The left column displays measurement results labeled as good, while the right column shows examples of results labeled as bad. Top, middle, and bottom rows correspond to individual gate characterizations, single-dot and double-dot measurements, respectively. All data used to train classifiers originates from devices other than those characterized and tuned here. The examples above stem from the device presented in Ref. [44].

readily available in PYTHON’s scikit-learn package: logistic regression, support vector machines (SVM), multilayer perceptron (MLP), Gaussian process, decision tree, random forest, quadratic discriminant analysis and  $k$ -nearest neighbors ( $k$ -NN). To estimate the potential of a model and to exclude overfitting, we average performances over  $n$  train and test splits. At each iteration, we first randomly select a subset with equal populations of all available data, i.e., equal numbers of good and poor results, and then split it into training and test sets. We use a percentage ratio of 80/20 between test and train data and we choose  $n = 20$  for 1D data and  $n = 10$  for 2D data based on performance fluctuation studies detailed in Appendix A.

Classification performances are evaluated using the accuracy score (ACC), defined as the ratio of correctly classified samples over the total number of samples. In machine-learning terms, the correctly labeled samples are the sum of true-positive (TP) and true-negative (TN) predictions, while the total number of samples is the sum of all positive ( $P$ ) and all negative ( $N$ ) samples:

$$S_{\text{ACC}} = \frac{T_P + T_N}{P + N}. \quad (4)$$

We compare classifier performances trained and tested on differently preprocessed data. In addition to the normalized

current we use the current map’s Fourier transform as well as principle components determined by performing a principle component analysis (PCA) implemented in sklearn [47]. All transformations are applied to train, test, and prediction data before classification. Principle components are extracted and hence defined from train data, which is expressed as amplitudes of each of the components. Test and prediction data are projected onto these components and the amplitudes are used for prediction. We compare performances using just the normalized current, its Fourier transform or both, with and without PCA. Results are summarized in Sec. VII and detailed in Appendix B.

## V. DEVICE CHARACTERIZATION

The objective of device characterization is to choose devices suitable for tuning among a large number of unknown devices. It establishes a list of working gates and their pinch-off voltages  $V_i^L, V_i^T, V_i^H$ , providing a quality measure and enabling early device comparison. We implement a predefined sequence of measurements by using the individual gate-characterization module introduced in Sec. IV A, sweeping each gate individually and preprocessing the data for machine-learning classification.

The algorithm initializes all gates to their upper safety limit  $V_{\text{safe max}}$  and measures the saturation current  $A_{\max}$ . For a gate to create an entirely opaque barrier, a negative voltage on a second, opposite gate needs to be set. We use the top barrier to deplete the 2DEG in the upper half of the device and to facilitate a complete depletion. It is set to its negative safety limit  $V_{\text{safe min}}$ , which in ideal devices will not result in a reduced current through the device. A signal drop below  $0.8A_{\max}$  without additional gate voltages set on the lower barrier gates indicates the presence of offset charges on one or several of the remaining gates. In this case the top-barrier voltage is increased in steps of  $0.2V$  until the signal is above the desired threshold  $0.8A_{\max}$ . Safety ranges of all gates are shifted towards more positive values by  $0.5V$ .

The left, central, and right barrier as well as left and right plunger are characterized individually. An example of this process, performed on device 3.A, is shown in Fig. 5. The quality of measurement results is assessed by a binary classifier, differentiating between good and bad gate responses. If all responses are classified as good, meaning they feature a high amplitude, sharp transition, and zero pinch-off current, a device is declared as working and considered for double-dot tuning. This selective choice ensures the tunability of a large range of tunnel couplings during fine tuning, undertaken once the double-dot regime is found.

Devices classified as working are characterized further by establishing a valid range for the top barrier, defined as the voltage range in which the remaining barriers are able to deplete the 2DEG. This is determined by decreasing the top barrier’s voltage starting from zero and in steps of

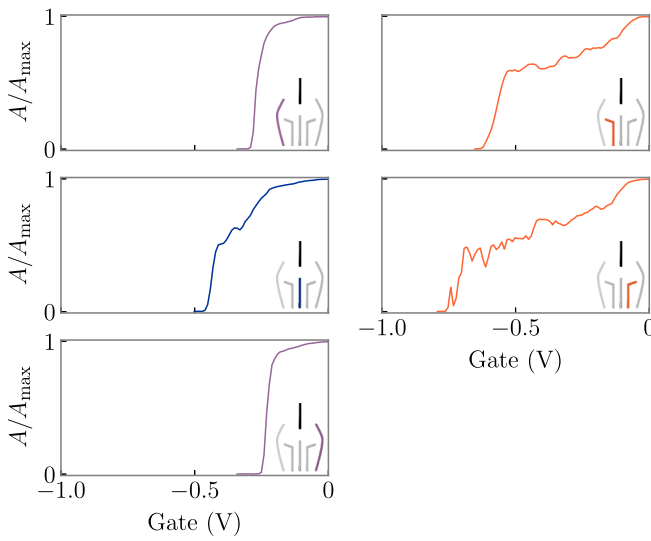


FIG. 5. Example of a device characterization. Normalized current is plotted as a function of gate voltage. The top barrier is set to its negative safety limit  $[V_{\text{TB}}^{\text{safe min}}, V_{\text{TB}}^{\text{safe max}}] = -3\text{V}$  and all remaining gates are characterized individually. In this case all gate responses are identified as good by the binary classifier, selecting the device for further tuning.

$0.2\text{V}$ , characterizing left, right, and central barrier at each iteration. If a barrier responds well, i.e., is able to deplete the 2DEG, it is not considered in subsequent iterations. The top-barrier voltage at which the last barrier is able to deplete the 2DEG defines the top barrier's lower valid range value  $V_{\text{TB}}^L$ . To establish the upper valid range voltage  $V_{\text{TB}}^H$ , the last barrier to pinch off is set to its lower safety limit  $V_{\text{safe min}}$  and the top barrier is characterized. The pinch-off voltage  $V^L$  defines  $V_{\text{TB}}^H$ . This step is specific to our device design and variances may need to be considered for other types of devices.

## VI. TUNING ALGORITHM

The purpose of the tuning algorithm is to tune fully working devices into either single- or double-dot regime. We illustrate the algorithm for the case of tuning into double-dot regime. It uses the same individual gate characterizations as in the previous section, but for a different top barrier. It determines suitable gate voltages of barriers and narrows down valid plunger ranges. The procedure used to determine the device's state and the next actions to take are illustrated in Fig. 6.

First, the algorithm initializes a given device by setting all its gates to their upper safety range  $V_{\text{safe max}}$  and measures the saturation current  $A_{\text{max}}$ . It then chooses a voltage for the top barrier. Values within  $[V_{\text{TB}}^L, V_{\text{TB}}^H]$  are considered promising values for a double-dot regime. In general, more positive top-barrier voltages are compensated for by more negative voltages on the remaining barriers later on.

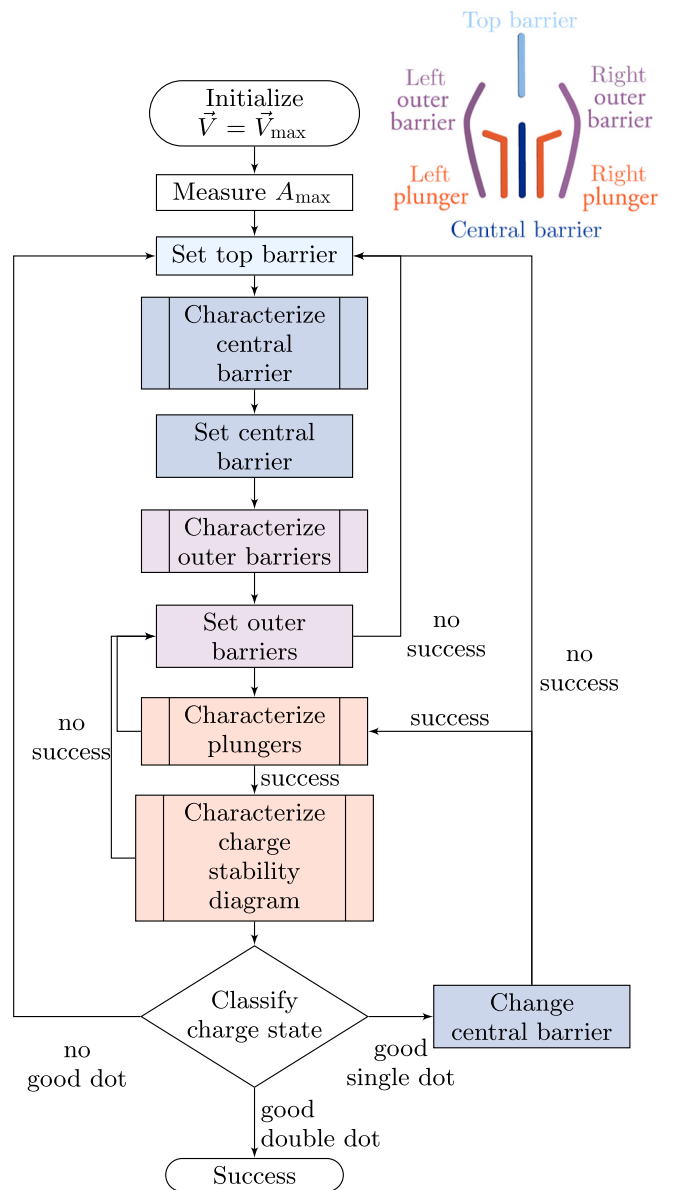


FIG. 6. Dot-tuning algorithm illustrated here for targeting a double-dot regime. Color encoding serves as a guide to which gates are characterized. Characterizing steps are implemented in software modules introduced in Sec. IV A and IV B. Individual gate characterization and charge-diagram modules are combined to tune working devices. No prior knowledge of valid voltages is assumed. Time-efficient 1D measurements determine suitable voltage values for barriers and narrow down valid ranges for plungers before measuring a 2D charge-stability diagram. Using three binary classifiers the quality and dot regime is predicted, based on which next tuning step is chosen.

Initially, the top barrier is set to

$$V_{\text{TB}} = V_{\text{TB}}^H - \frac{1}{4}(V_{\text{TB}}^H - V_{\text{TB}}^L), \quad (5)$$

at which the central barrier is characterized. Its initial value is set to the voltage corresponding to the current being at

75% of the saturation current,

$$A(V_{CB}) = 0.75A_{\max}. \quad (6)$$

The left and right barriers are characterized individually, with the respective other held at its highest allowed voltage. They are set to

$$V_i = V_i^L + \frac{1}{3}(V_i^H - V_i^L), \quad (7)$$

where  $i = \text{LB}, \text{RB}$ . The plungers' active voltage ranges  $[V_{LP}^L, V_{LP}^H], [V_{LP}^L, V_{LP}^H]$  are determined by individual gate characterizations before measuring a charge-stability diagram. The charge stability module adjusts plunger ranges to keep average currents within  $[0.004A_{\max}, 0.1A_{\max}]$ , as discussed in Sec. IV B. If this is not successful, meaning one or both plunger ranges reached the gate's safety limit, the respective neighboring outer barrier voltage is updated. The voltage change is calculated using the following rule:

$$\begin{aligned} \tilde{V}_i^\delta &= \begin{cases} 0.5(V_i^H - V_i), & \text{if current is too low} \\ 0.5(V_i - V_i^L), & \text{if current is too high} \end{cases} \\ V_i^\delta &= \min \left\{ 0.1, \max \left\{ \tilde{V}_i^\delta, 0.05 \right\} \right\}. \end{aligned} \quad (8)$$

The new barrier voltage  $V_i^{\text{new}}$  is then set to

$$V_i^{\text{new}} = \begin{cases} V_i + V_i^\delta, & \text{if current is too low} \\ V_i - V_i^\delta, & \text{if current is too high.} \end{cases} \quad (9)$$

If any of the outer barrier's new voltages are within  $0.1V$  of their safety range, a new top barrier is chosen. Using the same rule as above, the top barrier is set more negative if a lower safety limit has been reached, more positive otherwise.

If the charge-diagram module is successful in measuring a diagram with the desired current strength, classification of its segments guides further actions. If one or more segments have been classified as a good single dot, the algorithm adjusts the central barrier to more negative values using Eq. (9). Conversely, if aiming for single-dot regime and a segment is classified as a good double dot, the central-barrier voltage is increased. If this new value is within  $0.05V$  of the central barrier's safety range, the top barrier is changed instead, following the same rule as above. Unless the top barrier has changed, the algorithm resumes with plunger characterizations followed by a new charge diagram. If a new top-barrier voltage is set, it continues with outer barrier characterizations. If none of the segments features a good regime, the algorithm recommences by choosing a different initial top barrier. If the average current of the last charge diagram is below  $0.15A_{\max}$  of the saturation current, the new value is chosen more positive using Eq. (9), more negative otherwise.

The algorithm stops when at least one segment of the charge diagram is classified as the desired dot regime. We find it useful to continue iterating after finding the right regime for the first time, as the algorithm often finds even better defined double dots in subsequent iterations. Examples of this are shown in Figs. 11 and 12, which display two full tune ups, including additional iterations and charge-stability diagrams.

## VII. RESULTS

To test our characterization and tuning algorithms we use 12 double quantum-dot devices over two thermal cycles. An example of a device characterization is shown in Fig. 5 and a successful tune up resulting in double-dot regime in Fig. 7.

Of the six pairs of devices on our chip, we bond the four pairs in the corners: 1.A, 1.B, 3.A, 3.B, 4.A, 4.B, 6.A, 6.B, as shown in Fig. 2(c). Devices 6.A and 6.B do not have currents above noise level in either of the two cooldowns. These are thus identified as broken, which is either due to a contact failure within the device or within the wiring of the experimental setup. Each of the remaining devices are first characterized using five individual gate-characterization steps and classified using a binary classifier. Device 1.B is identified as broken as no gate is able to pinch off due to an unresponsive top barrier, and hence is not tuned. All remaining devices are tuned using the dot-tuning algorithm and all but two tune ups successfully reach the double-dot regime within the set number of iterations. Dielectric charging impeded tunability of devices 4.A and 4.B in the first cooldown, these runs are stopped before reaching the maximum number of 2D measurements allowed for tuning. We are also not able to tune these devices manually, however both recovered after a thermal cycle.

The tuning results as well as the number of 1D and 2D measurements required to complete the tasks are summarized in Table II. The number of 1D and 2D measurements for dot tuning vary from short tune ups of five 1D and one 2D measurements to fifteen and six, respectively. Using a lock-in excitation voltage to measure dc transport through the device, 1D measurements take 20–90 s each, while 2D measurements take approximately 25 min each.

Automation also allows us to easily study the evolution of device characteristics over time, tuning iterations, thermal cycles, or other experimental variables. As an example, we show in Fig. 8 the evolution of individual gate characterizations over three consecutive characterization and tuning iterations. We find that while the outer barriers do not change significantly, the central barrier and plungers show a large variation between the first and second tuning and a smaller variation between the second and third tuning. We speculate that electronic defects within the heterostructure become passivated during the

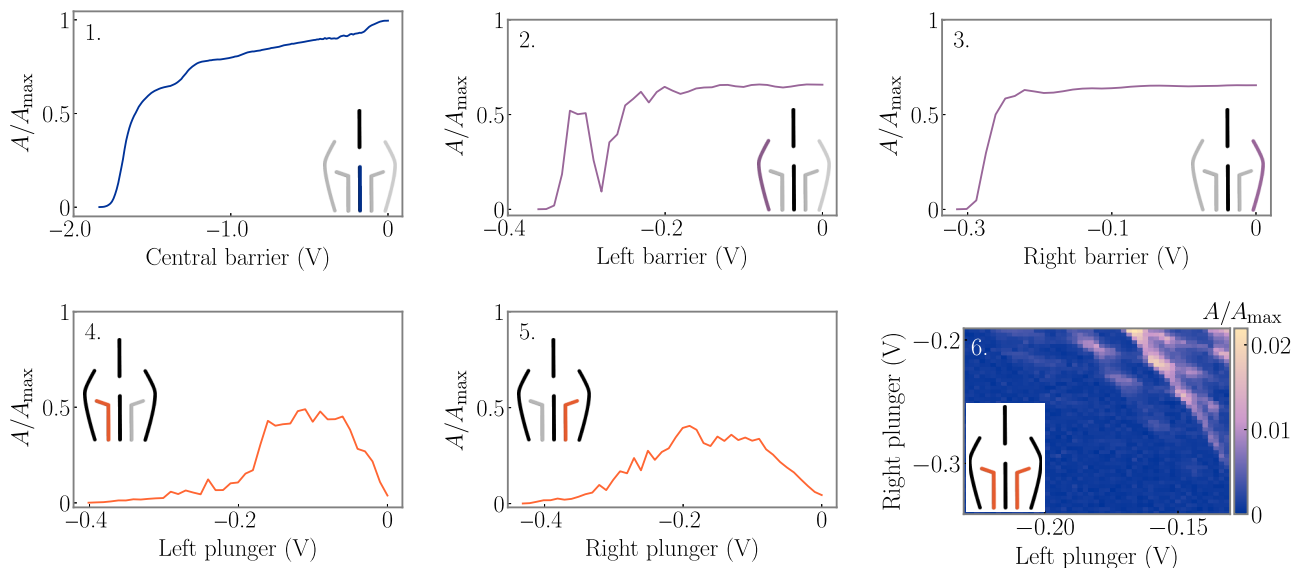


FIG. 7. Example of a successful tune up. The sequence shows the entire tune up of device 3.B during the second cooldown, as listed in Table II. The normalized current, amplitude  $A/A_{\max}$ , is plotted as a function of gate voltage and the device schemes in the insets indicate which gates are swept, with inactive gates set to  $0V$  marked in gray. Based on the top barrier's initial valid range, it is set to  $V_{TB} = -1.4V$  before characterizing the remaining gates. The central barrier is set to  $V_{CB} = -1.3444V$ , the left barrier to  $V_{LB} = -0.2776V$  and the right barrier to  $V_{RB} = -0.25753V$ . Plunger ranges are narrowed down to  $[V_{LP}^L, V_{LP}^H] = [-0.2006, -0.1304]V$ ,  $[V_{RP}^L, V_{RP}^H] = [-0.3411, -0.1906]V$  before measuring a charge diagram shown in the bottom-right figure. Using binary classifiers it is identified as a good double-dot regime, the required condition to stop the tuning procedure.

first tuning iteration, and that further iterations have a smaller effect. The number of iterations needed to reach stability depends on the active area of the channel between two gates being pinched off. This explains the observed differences between outer barriers, the central barrier, and plungers over successive tunings.

To determine the best classifier for quantum-dot tuning, we compare performances of logistic regression, support vector machines, multilayer perceptron, Gaussian process, decision tree, random forest, quadratic discriminant analysis and  $k$ -nearest neighbors for various input data: normalized current map and/or its Fourier transform and with

TABLE II. Summary of initial quality assessment (IQA), device characterization, and dot tuning of all devices measured. Device characterization of the first cooldown include two additional individual gate characterizations to determine a suitable top barrier to set. These sweeps are made redundant in the final characterization algorithm by simply using the top barrier's lower safety limit  $V_{TB}^{\text{safe min}}$  instead. Device 1.B is correctly identified as broken and thus not tuned. Devices 4.A and 4.B do not reach the desired dot regime in the first cooldown due to dielectric charging, which impedes tunability. These runs are stopped manually before reaching the maximum number of measurements allowed for tuning. However, both devices recovered after a thermal cycle. Devices 6.A and 6.B do not pass the initial quality assessment due to a lack of current through the device. The number of measurements needed to establish valid top-barrier ranges during the second stage of device characterization, which can be omitted in other device designs, range from 11 to 25 gate characterizations. Using standard lock-in techniques, it takes between 20 and 90 s to measure a 1D gate characterization and approximately 25 min to establish a charge-stability diagram.

Device	IQA	Cooldown 1						Cooldown 2					
		Characterization		Tuning			IQA	Characterization		Tuning			
		$n_{1D}$	Quality	$n_{1D}$	$n_{2D}$	Success		$n_{1D}$	Quality	$n_{1D}$	$n_{2D}$	Success	
1.A	✓	5(+2)+ 16	✓	13	5	✓	✓	5 + 15	✓	15	6	✓	
1.B	✓	5(+2) + -	✗	-	-	-	✓	5 + -	✗	-	-	-	
3.A	✓	5(+2)+ 19	✓	7	2	✓	✓	5 + 13	✓	11	5	✓	
3.B	✓	5(+2)+ 20	✓	7	2	✓	✓	5 + 15	✓	5	1	✓	
4.A	✓	5(+2)+ 11	✓	59	19	✗	✓	5 + 14	✓	11	4	✓	
4.B	✓	5(+2)+ 12	✓	21	9	✗	✓	5 + 14	✓	15	6	✓	
6.A	✗	-	-	-	-	-	✗	-	-	-	-	-	
6.B	✗	-	-	-	-	-	✗	-	-	-	-	-	

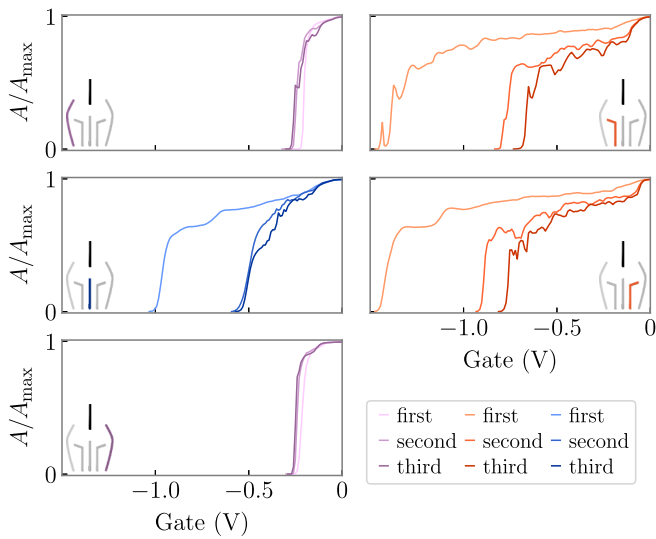


FIG. 8. Evolution of individual gate characterizations over three consecutive characterization and tuning iterations. Light colors correspond to the first tuning of the cooldown, medium dark and dark to the second and third, respectively. The device schemes in the insets indicate which gates are swept, with inactive gates set to  $0\text{ V}$  marked in gray. The top-barrier voltage is  $V_{\text{TB}}^{\text{safe min}} = -3\text{ V}$  for all sweeps. Pinch-off voltages of outer barriers do not change significantly, while the central barrier and both plungers show variations, which decrease at each consecutive run.

or without PCA. The results are detailed in Appendix B and show that performances reach up to 95% test accuracy for individual gate characterizations but stay below 90% for charge-state detection. Using principle components as input data either does not effect or decrease accuracy while not significantly improving train and prediction times for any category. Based on these results we choose the decision tree classifier applied to features to predict gate responses of individual gate characterizations. To assess the charge state of a charge-stability diagram we use all three classifiers to determine three possible outcomes: good single dot, good double dot, or no dot. We use the redundancy to overcome low-accuracy scores of individual classifiers. First, single, and double-dot quality classifiers assess whether a good charge state is present: if both outcomes are negative, there is no dot. If one is positive, the good regime it is indicating is present and if both predict good regimes the dot-regime classifier establishes a clear outcome.

The multilayer perceptron classifier performs best on all three charge-state classification categories. Single- and double-dot qualities are best predicted using both current maps and their Fourier transform. Dot-regime classification performs equally well on FT alone, suggesting that the FT captures the charge transitions' pattern differences of single- and double-dot regimes. This is not unexpected as a single dot gives rise to one-dimensional periodic

structures while double dots give rise to two-dimensional periodic structures.

### VIII. CONCLUSION

The tuning algorithm presented here establishes an autonomous procedure to tune gate-defined quantum dots, facilitating qubit initialization. This paves the way for quantum scale up in quantum-dot systems, where the growing chip size and complexity make manual-tuning procedures impractical. By automating well-established manual-tuning procedures and using binary classifiers to transfer scientists' knowledge of quantum-dot devices, we implement an autonomous two-stage device characterization and dot-tuning process. These algorithms enable characterization and tuning of devices in parallel and on a large scale without any premeasured input.

While we are able to successfully tune a range of devices across various scenarios, there are many opportunities for further improvements. Finding the double-dot regime can be a starting point for a subsequent local search to optimize the quality of the double dot. Fitting to a capacitance model can also be used during this search.

In order to make semiconductor qubit initialization fully autonomous from cooldown to qubit operation, setup-specific measurement initialization and calibration need to be addressed, as well as failure handling. Existing automation efforts, such as tuning into the single-electron regime [31,32], the fine tuning of the interdot tunnel couplings and virtual gate definition [24,48] can then also be integrated into our workflow.

Taking advantage of multiplexing technologies allows us to characterize more devices without being limited by the number of control lines. Replacing slow lock-in measurements by high-frequency charge sensing decreases run times and noise, while frequency multiplexing further improves throughput [49]. Turning to other measurement techniques requires appropriate feature selection and data preprocessing to ensure correct charge-regime classification, similar to what is implemented here.

Deeper investigations into feature selection, including voltage resolution and segment size, classifier choice and hyper-parameter optimization makes tuning more reliable. Understanding why some classifiers perform better than others and which features represent data best enables improved prediction accuracy. More sophisticated models in combination with boosting [50] may lead to further improvements.

Labeling errors, partially due to ambiguities between experts, and the vast variety of noise and charge states demands extensive data to capture most measurement outcomes. As this noise is difficult to simulate, classifiers need to be trained with real, not simulated data. This enables us to distinguish between noisy and intermediate charge states, a distinction not captured by classifiers trained

with ideal single- and double-dot charge diagrams. This is especially relevant if we wish to design new classifiers assessing specific tuning failures or fabrication defects.

Our procedure can be applied to other quantum-dot designs, including ones based on nanowires by neglecting the top barrier. The structure of both algorithms is general and can be applied to different materials by making minor changes to the parameters of the algorithms or inverting the polarity of the tuning procedure for holes [51,52].

The characterization procedure can also be extended to enable material and fabrication optimization, for example, by comparing pinch-off voltages or adding gate characterizations' sweeping voltages in opposite direction to assess hysteresis. The tuning procedure can be modified to account for more complex devices, such as multidot arrays and topological quantum-dot structures [53–55] or generalized to account for new physical phenomena such as zero-bias peaks or finding the topological phase [56,57].

As this field grows and more measurement data becomes available, there is an opportunity to take advantage of more complex machine-learning techniques such as reinforcement learning and Bayesian inference [58–60].

Going beyond device tuning, machine learning may have applications in areas as diverse as device design, fabrication optimization, measurement, and readout improvements or to optimize qubit control and feedback.

## ACKNOWLEDGMENTS

We thank Alice C. Mahoney, John M. Hornibrook, Rachpon Kalra, and Xanthe G. Croot for technical assistance and Christopher E. Granade, John K. Gamble, Charles M. Marcus, and David J. Reilly for helpful discussions and critical feedback. This research is supported by the Microsoft Corporation and the Australian Research Council Centre of Excellence for Engineered Quantum Systems (EQUS, CE170100009). The authors acknowledge the facilities as well as the scientific and technical assistance of the Research & Prototype Foundry Core Research Facility at the University of Sydney, part of the Australian National Fabrication Facility.

## APPENDIX A: METRIC FLUCTUATIONS

In Fig. 9 we show the dependence of the classifier performance on the number of redraws during training and testing. Based on this data we choose to average over  $n = 20$  redraws for individual gate characterization and  $n = 20$  for charge-state classification.

## APPENDIX B: CLASSIFIER CHOICE

We study classifier performance in three stages. First we compare performances of 12 classifiers, namely decision tree, Gaussian process, quadratic discriminant analysis, random forest, multilayer perceptron, logistic regression,

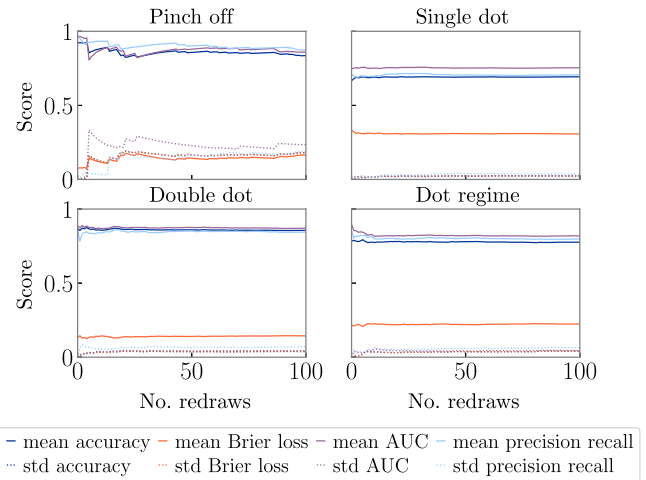


FIG. 9. Classifier performance dependence on the number of redraws during training and testing. Performance of support vector machines on pinch-off, single-dot, and double-dot current maps are evaluated over an increasing number of train and test data selection among the available data. Performances vary for a small number of iterations for individual gate-characterization data while they do not change much for charge-stability-diagram data. We choose to average individual gate-characterizations quality classification over  $n = 20$  times and charge-stability-diagram quality and state prediction over  $n = 10$ .

support vector machines, and  $k$ -nearest neighbors. We compute performances by comparing accuracy, which is defined as the total number of samples [true positive ( $T_P$ ) and true negative ( $T_N$ )] over the total number of samples

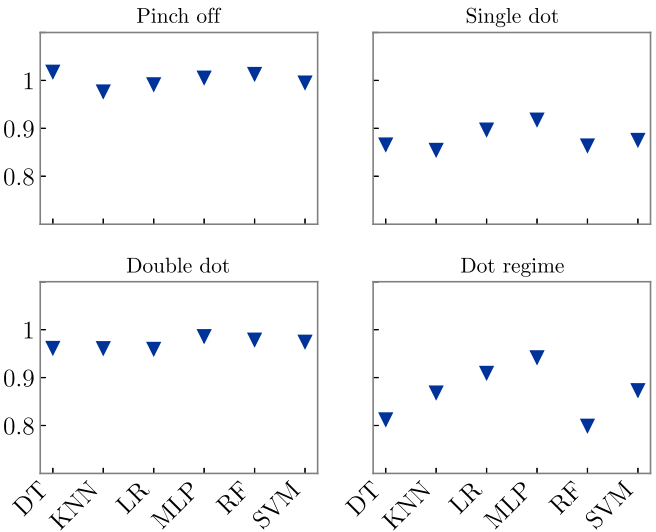


FIG. 10. Accuracies of optimized classifiers for individual gate characterizations (pinch off), single-dot, double-dot, and dot regime. Performances are high for pinch-off curves and double-dot quality and relatively low for single-dot quality and dot regime.

TABLE III. Optimized hyper parameters for the decision tree classifier determined by performing a grid search over one train and test split.

Hyper parameter	Pinch off	Single dot	Double dot	Dot regime
Criterion	Gini	Entropy	Entropy	Entropy
Max features	Auto	None	sqrt	Auto
Min samples leaf	2	3	3	1
Min samples split	6	2	6	2
Splitter	Random	Best	Best	Random
Accuracy	0.928571	0.755768	0.861027	0.767372

TABLE IV. Optimized hyper parameters for the  $k$ -nearest neighbor classifier determined by performing a grid search over one train and test split.

Hyper parameter	Pinch off	Single dot	Double dot	Dot regime
Algorithm	Auto	Auto	Auto	Auto
Leaf size	10	10	10	10
$n$ jobs	-1	-1	-1	-1
$n$ neighbors	2	2	2	2
$p$	3	2	1	2
Weights	Distance	Distance	Distance	Uniform
Accuracy	0.912698	0.790772	0.903323	0.81571

TABLE V. Optimized hyper parameters for the logistic regression classifier determined by performing a grid search over one train and test split.

Hyper parameter	Pinch off	Single dot	Double dot	Dot regime
C	100	0.1	1000	0.1
Class weight	Balanced	None	Balanced	Balanced
Fit intercept	True	True	True	True
Max iter	1000	1000	1000	1000
$n$ jobs	-1	-1	-1	-1
Penalty	l1	l1	l2	l2
Solver	Liblinear	Liblinear	Newton-cg	sag
Accuracy	0.92381	0.820207	0.897281	0.836858

TABLE VI. Optimized hyper parameters for the multilayer perceptron classifier determined by performing a grid search over one train and test split.

Hyper parameter	Pinch off	Single dot	Double dot	Dot regime
Activation	Relu	Relu	Logistic	Relu
Alpha	0.0001	0.1	0.001	0.001
Batch size	100	300	200	200
Hidden layer sizes	[100]	[100]	[200]	[300]
Learning rate	Constant	Adaptive	Invscale	Constant
Max iter	3000	3000	3000	3000
Power $t$	0.1	0.6	0.6	0.4
Solver	lbfgs	sgd	lbfgs	sgd
Accuracy	0.94127	0.845664	0.936556	0.876133

TABLE VII. Optimized hyper parameters for the random forest classifier determined by performing a grid search over one train and test split.

Hyper parameter	Pinch off	Single dot	Double dot	Dot regime
Criterion	Gini	Entropy	Entropy	Gini
Max features	Auto	sqrt	Auto	log2
Min samples leaf	1	2	1	2
Min samples split	6	4	2	2
$n$ estimators	10	500	100	100
$n$ jobs	-1	-1	-1	-1
Accuracy	0.950794	0.833731	0.918429	0.818731

TABLE VIII. Optimized hyper parameters for the Support Vector Machine determined by performing a grid search over one train and test split.

Hyper parameter	Pinch off	Single dot	Double dot	Dot regime
$C$	1000	0.1	0.1	10
Gamma	1	0.1	0.1	0.1
Kernel	rbf	Poly	Poly	Linear
Accuracy	0.94127	0.786794	0.879154	0.776435

[all positive ( $P$ ) and all negative ( $N$ )]:

$$S_{\text{ACC}} = \frac{T_P + T_N}{P + N}. \quad (\text{B1})$$

The accuracy is determined over  $n$  train and test splits of all available training data, selected randomly and with equal population sizes, i.e., equal numbers of good and

TABLE IX. Classifier performances on individual gate characterisations performed (from bottom to top) on normalized current, Fourier transform, both and selected features and with and without PCA. Accuracies were computed over  $n = 20$  train and test splits of the available data.

Classifier	PCA		No PCA	
	Accuracy	Evaluation time [s]	Accuracy	Evaluation time [s]
Normalized current				
Decision tree	$0.889 \pm 0.139$	$0.0001 \pm 0.0000$	$0.849 \pm 0.155$	$0.0001 \pm 0.0000$
Gaussian process	$0.854 \pm 0.180$	$0.0266 \pm 0.0012$	$0.847 \pm 0.188$	$0.0052 \pm 0.0010$
$k$ -nearest neighbors	$0.925 \pm 0.013$	$0.0222 \pm 0.0022$	$0.875 \pm 0.085$	$0.0075 \pm 0.0003$
Logistic regression	$0.879 \pm 0.136$	$0.0001 \pm 0.0000$	$0.877 \pm 0.136$	$0.0001 \pm 0.0000$
Multilayer perceptron	$0.887 \pm 0.140$	$0.0005 \pm 0.0001$	$0.833 \pm 0.187$	$0.0003 \pm 0.0001$
Quadratic discriminant analysis	$0.857 \pm 0.025$	$0.0009 \pm 0.0001$	$0.803 \pm 0.184$	$0.0002 \pm 0.0000$
Random forest	$0.860 \pm 0.155$	$0.0010 \pm 0.0001$	$0.882 \pm 0.108$	$0.0010 \pm 0.0001$
Support vector machine	$0.846 \pm 0.169$	$0.0085 \pm 0.0074$	$0.884 \pm 0.133$	$0.0007 \pm 0.0003$
Fourier transform				
Decision tree	$0.909 \pm 0.018$	$0.0001 \pm 0.0000$	$0.891 \pm 0.029$	$0.0001 \pm 0.0000$
Gaussian process	$0.846 \pm 0.162$	$0.0263 \pm 0.0007$	$0.854 \pm 0.153$	$0.0109 \pm 0.0029$
$k$ -nearest neighbors	$0.867 \pm 0.035$	$0.0277 \pm 0.0012$	$0.871 \pm 0.046$	$0.0104 \pm 0.0012$
Logistic regression	$0.866 \pm 0.129$	$0.0001 \pm 0.0001$	$0.884 \pm 0.101$	$0.0001 \pm 0.0000$
Multilayer perceptron	$0.811 \pm 0.184$	$0.0005 \pm 0.0001$	$0.856 \pm 0.124$	$0.0004 \pm 0.0001$
Quadratic discriminant analysis	$0.810 \pm 0.029$	$0.0009 \pm 0.0001$	$0.722 \pm 0.093$	$0.0004 \pm 0.0001$
Random forest	$0.890 \pm 0.019$	$0.0012 \pm 0.0001$	$0.852 \pm 0.038$	$0.0010 \pm 0.0001$
Support vector machine	$0.853 \pm 0.151$	$0.0077 \pm 0.0062$	$0.863 \pm 0.144$	$0.0018 \pm 0.0003$
Normalized current & Fourier transform				
Decision tree	$0.929 \pm 0.021$	$0.0001 \pm 0.0000$	$0.904 \pm 0.031$	$0.0001 \pm 0.0000$
Gaussian process	$0.849 \pm 0.177$	$0.0523 \pm 0.0010$	$0.868 \pm 0.156$	$0.0094 \pm 0.0027$
$k$ -nearest neighbors	$0.899 \pm 0.033$	$0.0483 \pm 0.0033$	$0.902 \pm 0.052$	$0.0103 \pm 0.0014$
Logistic regression	$0.865 \pm 0.142$	$0.0001 \pm 0.0000$	$0.851 \pm 0.160$	$0.0001 \pm 0.0000$
Multilayer perceptron	$0.899 \pm 0.111$	$0.0007 \pm 0.0001$	$0.856 \pm 0.153$	$0.0004 \pm 0.0001$
Quadratic discriminant analysis	$0.810 \pm 0.022$	$0.0018 \pm 0.0001$	$0.843 \pm 0.115$	$0.0004 \pm 0.0001$
Random forest	$0.911 \pm 0.030$	$0.0011 \pm 0.0002$	$0.862 \pm 0.039$	$0.0010 \pm 0.0001$
Support vector machine	$0.798 \pm 0.192$	$0.0214 \pm 0.0186$	$0.849 \pm 0.171$	$0.0018 \pm 0.0004$
Selected features				
Decision tree	$0.928 \pm 0.020$	$0.0001 \pm 0.0000$	$0.921 \pm 0.028$	$0.0001 \pm 0.0000$
Gaussian process	$0.922 \pm 0.024$	$0.0023 \pm 0.0002$	$0.919 \pm 0.027$	$0.0025 \pm 0.0002$
$k$ -nearest neighbors	$0.896 \pm 0.040$	$0.0064 \pm 0.0005$	$0.898 \pm 0.033$	$0.0052 \pm 0.0002$
Logistic regression	$0.916 \pm 0.021$	$0.0001 \pm 0.0000$	$0.904 \pm 0.037$	$0.0001 \pm 0.0000$
Multilayer perceptron	$0.927 \pm 0.023$	$0.0002 \pm 0.0000$	$0.917 \pm 0.029$	$0.0002 \pm 0.0000$
Quadratic discriminant analysis	$0.872 \pm 0.037$	$0.0002 \pm 0.0000$	$0.870 \pm 0.034$	$0.0001 \pm 0.0000$
Random forest	$0.939 \pm 0.024$	$0.0010 \pm 0.0001$	$0.933 \pm 0.018$	$0.0009 \pm 0.0001$
Support vector machine	$0.895 \pm 0.084$	$0.0012 \pm 0.0028$	$0.914 \pm 0.028$	$0.0005 \pm 0.0002$

TABLE X. Classifier performances on single-dot charge-stability diagrams performed (from bottom to top) on normalized current, Fourier transform and both and with and without PCA. Accuracies were computed over  $n = 10$  train and test splits of the available data.

Classifier	PCA		No PCA	
	Accuracy	Evaluation time [s]	Accuracy	Evaluation time [s]
	Normalized current			
Decision tree	$0.743 \pm 0.030$	$0.0015 \pm 0.0001$	$0.737 \pm 0.025$	$0.0001 \pm 0.0000$
Gaussian process	$0.732 \pm 0.032$	$1.1919 \pm 0.0082$	$0.741 \pm 0.020$	$0.0261 \pm 0.0013$
$k$ -nearest neighbors	$0.676 \pm 0.026$	$1.0636 \pm 0.0255$	$0.727 \pm 0.030$	$0.0182 \pm 0.0004$
Logistic regression	$0.717 \pm 0.021$	$0.0006 \pm 0.0000$	$0.753 \pm 0.021$	$0.0001 \pm 0.0000$
Multilayer perceptron	$0.752 \pm 0.027$	$0.0038 \pm 0.0002$	$0.755 \pm 0.022$	$0.0004 \pm 0.0000$
Quadratic discriminant analysis	$0.559 \pm 0.020$	$0.0418 \pm 0.0017$	$0.766 \pm 0.019$	$0.0004 \pm 0.0001$
Random forest	$0.763 \pm 0.025$	$0.0026 \pm 0.0001$	$0.697 \pm 0.027$	$0.0011 \pm 0.0000$
Support vector machine	$0.693 \pm 0.023$	$0.6249 \pm 0.0188$	$0.759 \pm 0.022$	$0.0108 \pm 0.0005$
Fourier transform				
Decision tree	$0.689 \pm 0.020$	$0.0016 \pm 0.0001$	$0.661 \pm 0.024$	$0.0002 \pm 0.0000$
Gaussian process	$0.637 \pm 0.022$	$1.2200 \pm 0.0110$	$0.661 \pm 0.030$	$0.2101 \pm 0.0085$
$k$ -nearest neighbors	$0.688 \pm 0.023$	$1.5608 \pm 0.0284$	$0.682 \pm 0.034$	$0.2085 \pm 0.0083$
Logistic regression	$0.699 \pm 0.030$	$0.0006 \pm 0.0001$	$0.707 \pm 0.024$	$0.0001 \pm 0.0000$
Multilayer perceptron	$0.741 \pm 0.023$	$0.0037 \pm 0.0003$	$0.733 \pm 0.021$	$0.0009 \pm 0.0000$
Quadratic discriminant Analysis	$0.541 \pm 0.026$	$0.0403 \pm 0.0013$	$0.696 \pm 0.020$	$0.0060 \pm 0.0004$
Random forest	$0.686 \pm 0.024$	$0.0031 \pm 0.0000$	$0.585 \pm 0.026$	$0.0013 \pm 0.0001$
Support vector machine	$0.665 \pm 0.025$	$0.5690 \pm 0.0185$	$0.693 \pm 0.026$	$0.0869 \pm 0.0042$
Normalized current & Fourier transform				
Decision tree	$0.752 \pm 0.027$	$0.0025 \pm 0.0003$	$0.738 \pm 0.035$	$0.0003 \pm 0.0000$
Gaussian process	$0.679 \pm 0.025$	$2.4434 \pm 0.0123$	$0.700 \pm 0.021$	$0.1919 \pm 0.0071$
$k$ -nearest neighbors	$0.748 \pm 0.019$	$3.1041 \pm 0.0306$	$0.757 \pm 0.021$	$0.1542 \pm 0.0084$
Logistic regression	$0.797 \pm 0.016$	$0.0011 \pm 0.0001$	$0.797 \pm 0.022$	$0.0001 \pm 0.0000$
Multilayer perceptron	$0.820 \pm 0.017$	$0.0070 \pm 0.0003$	$0.795 \pm 0.021$	$0.0009 \pm 0.0001$
Quadratic discriminant analysis	$0.553 \pm 0.028$	$0.0819 \pm 0.0015$	$0.757 \pm 0.025$	$0.0059 \pm 0.0005$
Random forest	$0.765 \pm 0.024$	$0.0042 \pm 0.0002$	$0.567 \pm 0.041$	$0.0013 \pm 0.0001$
Support vector machine	$0.773 \pm 0.023$	$0.8536 \pm 0.0259$	$0.773 \pm 0.018$	$0.0577 \pm 0.0029$

poor results, where we choose  $n = 20$  for 1D data and  $n = 10$  for 2D. We compare how these classifiers perform with default hyper parameters and on different feature vectors, i.e., normalized current, Fourier transform, both or on extracted features if they are available. Based on this initial analysis we discard two poorly performing classifiers, quadratic discriminant analysis and Gaussian process. All remaining classifiers are then optimized using scikit-learn's selection.GridSearchCV [47] method to determine their hyper parameters  $h$ . The grid-search method evaluates all possible combinations of a supplied range of possible hyper parameters to select the optimal one. Given the long run times of this method we optimize each classifier for a single split of available data into train and test subsets. This slightly overestimates each classifier's performance as it optimizes hyper parameters to one train and test data split. We therefore compute performances of classifiers with their respective hyper parameters again and over  $n = 20$  and  $n = 10$  train and test data splits for pinch-off and charge-stability diagram data,

respectively. Based on these results we choose the decision tree classifier to predict pinch-off curves and the multilayer perceptron to determine charge-stability diagram quality and charge state. Lastly, we look at the confusion matrix of each of these classifiers, which is defined by the number of false positives ( $F_P$ ), false negatives ( $F_N$ ), true positives ( $T_P$ ), and true negatives ( $T_N$ ):

$$S_{CM} = \begin{pmatrix} T_P & F_P \\ F_N & T_N \end{pmatrix}. \quad (B2)$$

For pinch-off curves classified using a decision tree classifier we find

$$S_{CM, DT, \text{pinch off}} = \begin{pmatrix} 70.98 & 8.24 \\ 4.71 & 74.07 \end{pmatrix} \quad (B3)$$

$$S_{ACC, DT, \text{pinch off}} = 0.9181 \pm 0.0442,$$

TABLE XI. Classifier performances on double-dot charge-stability diagrams performed (from bottom to top) on normalized current, Fourier transform and both and with and without PCA. Accuracies were computed over  $n = 10$  train and test splits of the available data.

Classifier	PCA		No PCA	
	Accuracy	Evaluation time [s]	Accuracy	Evaluation time [s]
	Normalized current			
Decision tree	$0.848 \pm 0.052$	$0.0005 \pm 0.0001$	$0.873 \pm 0.043$	$0.0001 \pm 0.0000$
Gaussian process	$0.829 \pm 0.044$	$0.0924 \pm 0.0122$	$0.854 \pm 0.039$	$0.0071 \pm 0.0019$
$k$ -nearest neighbors	$0.802 \pm 0.065$	$0.0962 \pm 0.0079$	$0.830 \pm 0.040$	$0.0062 \pm 0.0011$
Logistic regression	$0.707 \pm 0.063$	$0.0002 \pm 0.0000$	$0.704 \pm 0.072$	$0.0001 \pm 0.0000$
Multilayer perceptron	$0.786 \pm 0.041$	$0.0021 \pm 0.0008$	$0.848 \pm 0.027$	$0.0006 \pm 0.0013$
Quadratic discriminant analysis	$0.575 \pm 0.080$	$0.0720 \pm 0.0064$	$0.743 \pm 0.062$	$0.0002 \pm 0.0000$
Random forest	$0.886 \pm 0.030$	$0.0019 \pm 0.0001$	$0.810 \pm 0.032$	$0.0011 \pm 0.0001$
Support vector machine	$0.686 \pm 0.059$	$0.0666 \pm 0.0041$	$0.674 \pm 0.057$	$0.0011 \pm 0.0004$
Fourier transform				
Decision tree	$0.767 \pm 0.046$	$0.0005 \pm 0.0001$	$0.753 \pm 0.045$	$0.0001 \pm 0.0000$
Gaussian process	$0.736 \pm 0.037$	$0.0863 \pm 0.0008$	$0.774 \pm 0.040$	$0.0128 \pm 0.0015$
$k$ -nearest neighbors	$0.780 \pm 0.043$	$0.1230 \pm 0.0059$	$0.785 \pm 0.050$	$0.0099 \pm 0.0012$
Logistic regression	$0.799 \pm 0.040$	$0.0002 \pm 0.0001$	$0.798 \pm 0.051$	$0.0011 \pm 0.0009$
Multilayer perceptron	$0.822 \pm 0.048$	$0.0019 \pm 0.0002$	$0.827 \pm 0.041$	$0.0041 \pm 0.0032$
Quadratic discriminant analysis	$0.572 \pm 0.054$	$0.0708 \pm 0.0056$	$0.700 \pm 0.084$	$0.0049 \pm 0.0035$
Random forest	$0.754 \pm 0.038$	$0.0020 \pm 0.0003$	$0.768 \pm 0.038$	$0.0011 \pm 0.0000$
Support vector machine	$0.792 \pm 0.042$	$0.0536 \pm 0.0047$	$0.796 \pm 0.033$	$0.0020 \pm 0.0009$
Normalized current & Fourier transform				
Decision tree	$0.867 \pm 0.035$	$0.0008 \pm 0.0001$	$0.851 \pm 0.043$	$0.0001 \pm 0.0002$
Gaussian process	$0.746 \pm 0.032$	$0.2306 \pm 0.0017$	$0.787 \pm 0.042$	$0.0111 \pm 0.0010$
$k$ -nearest neighbors	$0.853 \pm 0.049$	$0.2399 \pm 0.0471$	$0.859 \pm 0.031$	$0.0093 \pm 0.0010$
Logistic regression	$0.868 \pm 0.036$	$0.0004 \pm 0.0001$	$0.875 \pm 0.036$	$0.0013 \pm 0.0015$
Multilayer perceptron	$0.901 \pm 0.032$	$0.0033 \pm 0.0003$	$0.880 \pm 0.028$	$0.0041 \pm 0.0038$
Quadratic discriminant analysis	$0.568 \pm 0.066$	$0.1342 \pm 0.0103$	$0.795 \pm 0.048$	$0.0007 \pm 0.0003$
Random forest	$0.881 \pm 0.033$	$0.0022 \pm 0.0001$	$0.776 \pm 0.043$	$0.0011 \pm 0.0001$
Support vector machine	$0.852 \pm 0.045$	$0.0830 \pm 0.0070$	$0.862 \pm 0.032$	$0.0011 \pm 0.0001$

for single-dot charge-stability-diagram quality classified using a multilayer perceptron

$$S_{CM, \text{MLP, single dot}} = \begin{pmatrix} 129.5 & 29.25 \\ 28.05 & 128.2 \end{pmatrix} \quad (\text{B4})$$

$$S_{ACC, \text{MLP, single dot}} = 0.8181 \pm 0.0178,$$

for double-dot stability-diagram quality classified using a multilayer perceptron

$$S_{CM, \text{MLP, single dot}} = \begin{pmatrix} 37.72 & 3.84 \\ 5.6 & 35.84 \end{pmatrix} \quad (\text{B5})$$

$$S_{ACC, \text{MLP, single dot}} = 0.8863 \pm 0.0427,$$

and for dot regime of charge-stability diagrams classified using a multilayer perceptron:

$$S_{CM, \text{MLP, single dot}} = \begin{pmatrix} 33.95 & 7.45 \\ 5.65 & 35.95 \end{pmatrix} \quad (\text{B6})$$

$$S_{ACC, \text{MLP, single dot}} = 0.8422 \pm 0.0363.$$

The tables below summarize all intermediate performance evaluations as well as hyper-parameter optimization results. Final performances are illustrated in Fig. 10 and optimized hyper parameters with corresponding accuracy over one train and test data split in Table III to VIII, for the decision tree,  $k$ -nearest neighbor classifier, logistic regression, multilayer perceptron, random forest, and support vector machine classifier, respectively. Performances of classifiers with default hyper parameters are listed in Table IX for individual gate characterizations, Table X for single-dot quality, Table XI for double-dot quality, and Table XII for dot regime.

## APPENDIX C: TUNING EXAMPLES

We show tuning sequences of device 1.A and 3.A in Figs. 11 and 12 respectively. These sequences highlight the fact that once a good double-dot regime is found, further iterations of the algorithm may help improve the quality of the result.

TABLE XII. Classifier performances on good single-dot and good double-dot charge-stability diagrams performed (from bottom to top) on normalized current, Fourier transform and both and with and without PCA. Accuracies were computed over  $n = 10$  train and test splits of the available data.

Classifier	PCA		No PCA	
	Accuracy	Evaluation time [s]	Accuracy	Evaluation time [s]
	Normalized current			
Decision tree	$0.629 \pm 0.054$	$0.0005 \pm 0.0001$	$0.583 \pm 0.052$	$0.0001 \pm 0.0000$
Gaussian process	$0.625 \pm 0.047$	$0.1144 \pm 0.0008$	$0.666 \pm 0.042$	$0.0111 \pm 0.0016$
$k$ -nearest neighbors	$0.627 \pm 0.059$	$0.1753 \pm 0.0183$	$0.653 \pm 0.040$	$0.0102 \pm 0.0012$
Logistic regression	$0.626 \pm 0.037$	$0.0003 \pm 0.0001$	$0.623 \pm 0.049$	$0.0014 \pm 0.0013$
Multilayer perceptron	$0.658 \pm 0.047$	$0.0018 \pm 0.0002$	$0.665 \pm 0.046$	$0.0047 \pm 0.0026$
Quadratic discriminant analysis	$0.516 \pm 0.056$	$0.0698 \pm 0.0069$	$0.768 \pm 0.082$	$0.0007 \pm 0.0003$
Random forest	$0.601 \pm 0.048$	$0.0019 \pm 0.0002$	$0.563 \pm 0.050$	$0.0011 \pm 0.0001$
Support vector machine	$0.580 \pm 0.042$	$0.0700 \pm 0.0033$	$0.627 \pm 0.051$	$0.0027 \pm 0.0006$
Fourier transform				
Decision tree	$0.724 \pm 0.059$	$0.0004 \pm 0.0001$	$0.736 \pm 0.047$	$0.0001 \pm 0.0000$
Gaussian process	$0.782 \pm 0.031$	$0.1142 \pm 0.0012$	$0.776 \pm 0.041$	$0.0147 \pm 0.0016$
$k$ -nearest neighbors	$0.825 \pm 0.037$	$0.1717 \pm 0.0128$	$0.828 \pm 0.038$	$0.0157 \pm 0.0011$
Logistic regression	$0.816 \pm 0.044$	$0.0003 \pm 0.0001$	$0.798 \pm 0.051$	$0.0009 \pm 0.0006$
Multilayer perceptron	$0.838 \pm 0.030$	$0.0018 \pm 0.0001$	$0.837 \pm 0.040$	$0.0066 \pm 0.0043$
Quadratic discriminant analysis	$0.523 \pm 0.046$	$0.0713 \pm 0.0085$	$0.592 \pm 0.107$	$0.0010 \pm 0.0002$
Random forest	$0.695 \pm 0.051$	$0.0020 \pm 0.0002$	$0.637 \pm 0.043$	$0.0011 \pm 0.0001$
Support vector machine	$0.790 \pm 0.046$	$0.0469 \pm 0.0034$	$0.778 \pm 0.031$	$0.0024 \pm 0.0003$
Normalized current & Fourier transform				
Decision tree	$0.698 \pm 0.046$	$0.0008 \pm 0.0000$	$0.684 \pm 0.058$	$0.0001 \pm 0.0000$
Gaussian process	$0.669 \pm 0.054$	$0.2313 \pm 0.0020$	$0.699 \pm 0.041$	$0.0152 \pm 0.0020$
$k$ -nearest neighbors	$0.749 \pm 0.045$	$0.3904 \pm 0.0447$	$0.778 \pm 0.041$	$0.0215 \pm 0.0103$
Logistic regression	$0.798 \pm 0.035$	$0.0004 \pm 0.0000$	$0.789 \pm 0.038$	$0.0027 \pm 0.0027$
Multilayer perceptron	$0.836 \pm 0.035$	$0.0033 \pm 0.0001$	$0.820 \pm 0.053$	$0.0050 \pm 0.0036$
Quadratic discriminant analysis	$0.510 \pm 0.040$	$0.0894 \pm 0.0522$	$0.647 \pm 0.096$	$0.0010 \pm 0.0003$
Random forest	$0.684 \pm 0.055$	$0.0022 \pm 0.0001$	$0.607 \pm 0.049$	$0.0011 \pm 0.0001$
Support vector machine	$0.769 \pm 0.046$	$0.0753 \pm 0.0062$	$0.769 \pm 0.027$	$0.0026 \pm 0.0005$

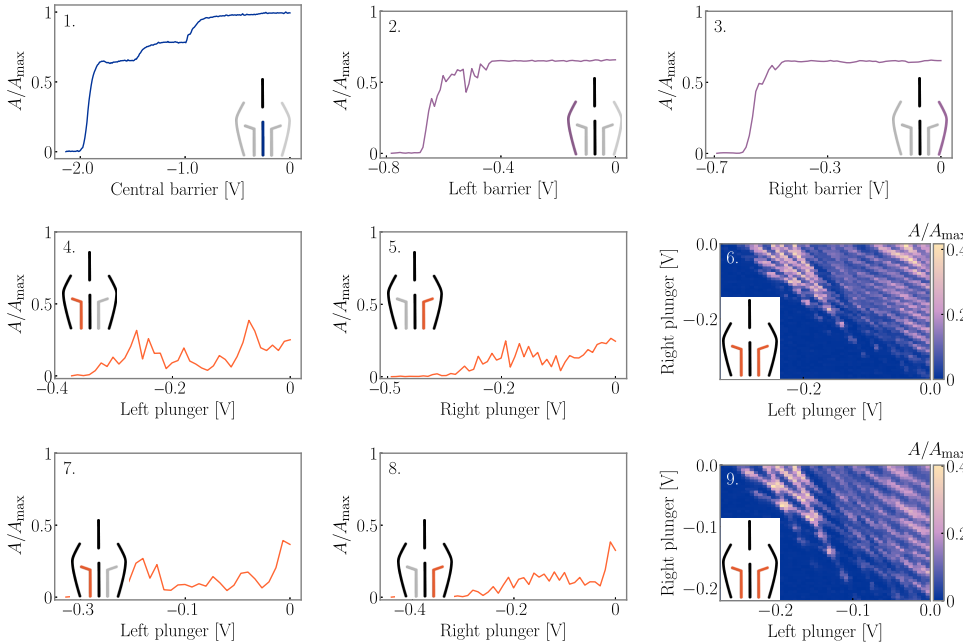


FIG. 11. Example of a successful tune up with one additional iteration of the tuning algorithm after the double-dot regime was found. The sequence shows the tune up of device 3.A during the first cooldown (see Table II). The normalized current, amplitude  $A/A_{\max}$ , is plotted as a function of gate voltage and the device schemes in the insets indicate which gates were swept with inactive gates set to  $0V$  marked in gray. While the algorithm found a good double-dot regime in the first 2D measurement, the second charge diagram features brighter and sharper triple points.

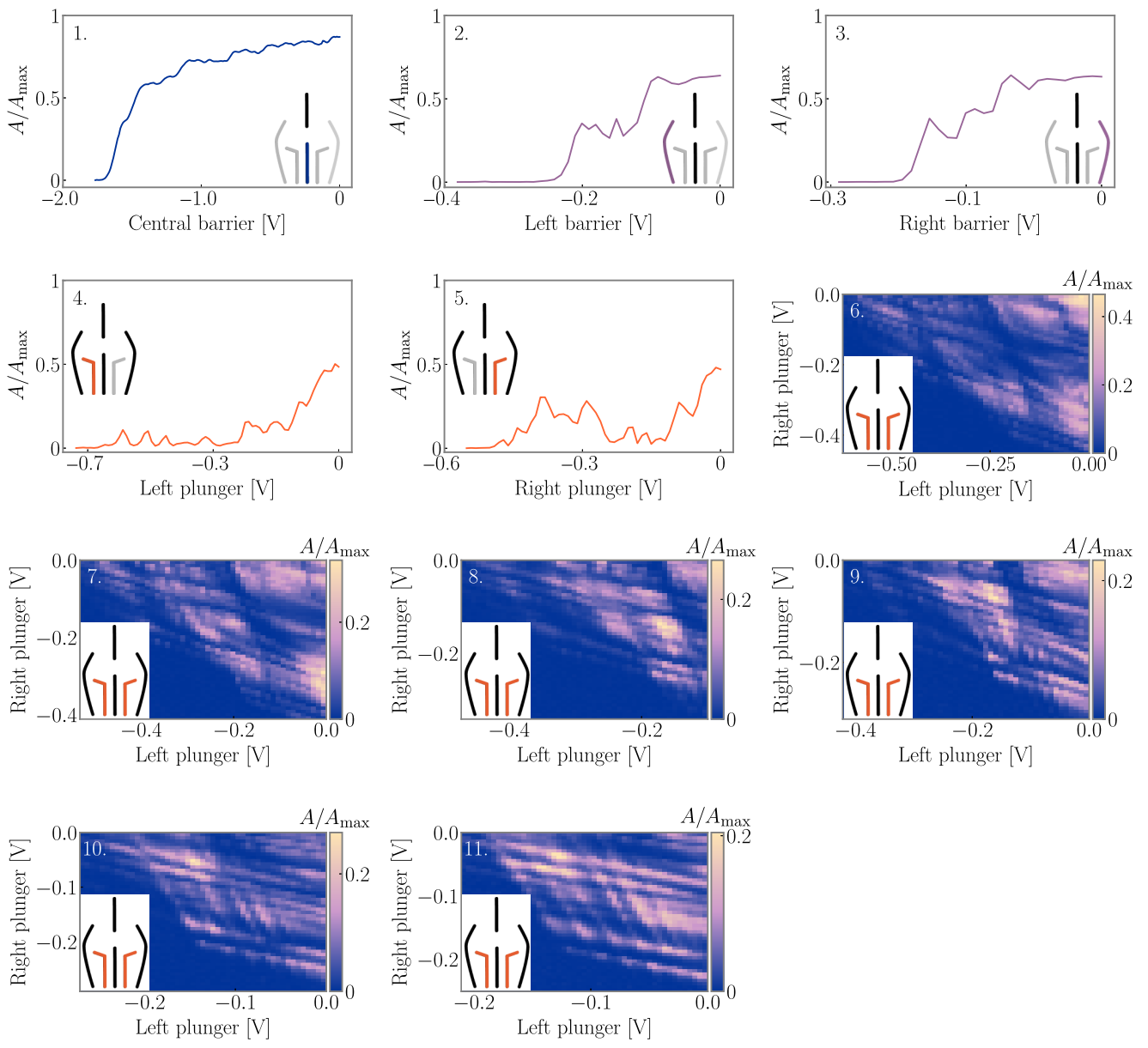


FIG. 12. Example of a successful tune up with additional iterations of the tuning algorithm after the double-dot regime is found. The sequence shows the tune up of device 1.A during the first cooldown (see Table II). The normalized current, amplitude  $A/A_{\max}$ , is plotted as a function of gate voltage and the device schemes in the insets indicate which gates are swept with inactive gates set to 0V marked in gray. The fourth charge-stability diagram (measurement 9) shows a good double-dot regime, which is then improved by two subsequent tuning iterations, setting the central barrier more negative. These charge-stability diagrams feature sharper triple points and clearer transitions. Two 1D measurements, one for each plunger gate and similar to measurements 4 and 5 above, are taken in between charge-stability diagrams 6–11. These measurements are omitted here for clarity.

- [1] Peter W. Shor, Polynomial-time algorithms for prime factorization and discrete logarithms on a quantum computer, *SIAM J. Comput.* **26**, 1484 (1997).
- [2] Markus Reiher, Nathan Wiebe, Krysta M. Svore, Dave Wecker, and Matthias Troyer, Elucidating reaction mechanisms on quantum computers, *Proc. Natl. Acad. Sci. U.S.A.* **29**, 7555 (2017).
- [3] Dave Wecker, Matthew B. Hastings, Nathan Wiebe, Bryan K. Clark, Chetan Nayak, and Matthias Troyer, Solving

strongly correlated electron models on a quantum computer, *Phys. Rev. A* **92**, 062318 (2015).

- [4] I. Rungger, N. Fitzpatrick, H. Chen, C. H. Alderete, H. Apel, A. Cowtan, A. Patterson, D. Munoz Ramo, Y. Zhu, N. H. Nguyen, E. Grant, S. Chretien, L. Wossnig, N. M. Linke, and R. Duncan, Dynamical mean field theory algorithm and experiment on quantum computers (2019), arXiv:1910.04735.
- [5] J. Zhang, G. Pagano, P. W. Hess, A. Kyprianidis, P. Becker, H. Kaplan, A. V. Gorshkov, Z.-X. Gong, and C. Monroe, Observation of a many-body dynamical phase transition

- with a 53-qubit quantum simulator, *Nature* **551**, 601 (2017).
- [6] A. Chiesa, F. Tacchino, M. Grossi, P. Santini, I. Tavernelli, D. Gerace, and S. Carretta, Quantum hardware simulating four-dimensional inelastic neutron scattering, *Nat. Phys.* **15**, 455 (2019).
- [7] Craig S. Hamilton, Regina Kruse, Linda Sansoni, Sonja Barkhofen, Christine Silberhorn, and Igor Jex, Gaussian Boson Sampling, *Phys. Rev. Lett.* **119**, 170501 (2017).
- [8] John Preskill, Quantum computing in the NISQ era and beyond, *Quantum* **2**, 79 (2018).
- [9] Frank Arute, Kunal Arya, Ryan Babbush, Dave Bacon, Joseph C. Bardin, Rami Barends, Rupak Biswas, Sergio Boixo, Fernando G. S. L. Brandao, David A. Buell, Brian Burkett, Yu Chen, Zijun Chen, Ben Chiaro, Roberto Collins, others., Quantum supremacy using a programmable superconducting processor, *Nature* **574**, 505 (2019).
- [10] K. D. Petersson, J. R. Petta, H. Lu, and A. C. Gossard, Quantum Coherence in a One-Electron Semiconductor Charge Qubit, *Phys. Rev. Lett.* **105**, 246804 (2010).
- [11] J. Gorman, D. G. Hasko, and D. A. Williams, Charge-Qubit Operation of an Isolated Double Quantum Dot, *Phys. Rev. Lett.* **95**, 090502 (2005).
- [12] Yuan-Chi Yang, S. N. Coppersmith, and Mark Friesen, Achieving high-fidelity single-qubit gates in a strongly driven charge qubit with 1/f charge noise, *npj Quantum Inf.* **5**, 12 (2019).
- [13] Daniel Loss, and David P. DiVincenzo, Quantum computation with quantum dots, *Phys. Rev. A* **57**, 120 (1998).
- [14] R. Hanson, L. P. Kouwenhoven, J. R. Petta, S. Tarucha, and L. M. K. Vandersypen, Spins in few-electron quantum dots, *Rev. Mod. Phys.* **79**, 1217 (2007).
- [15] J. R. Petta, A. C. Johnson, J. M. Taylor, E. A. Laird, A. Yacoby, M. D. Lukin, C. M. Marcus, M. P. Hanson, and A. C. Gossard, Coherent manipulation of coupled electron spins in semiconductor quantum dots, *Science* **309**, 2180 (2005).
- [16] M. Veldhorst, C. H. Yang, J. C. C. Hwang, W. Huang, J. P. Dehollain, J. T. Muhonen, S. Simmons, A. Laucht, F. E. Hudson, K. M. Itoh, A. Morello, and A. S. Dzurak, A two-qubit logic gate in silicon, *Nature* **526**, 410 (2015).
- [17] A. Y. Kitaev, Unpaired Majorana fermions in quantum wires, *Physics-Uspekhi* **44**, 131 (2001).
- [18] Torsten Karzig, Christina Knapp, Roman M. Lutchyn, Parsa Bonderson, Matthew B. Hastings, Chetan Nayak, Jason Alicea, Karsten Flensberg, Stephan Plugge, Yuval Oreg, Charles M. Marcus, and Michael H. Freedman, Scalable designs for quasiparticle-poisoning-protected topological quantum computation with Majorana zero modes, *Phys. Rev. B* **95**, 235305 (2017).
- [19] Jason Alicea, Yuval Oreg, Gil Refael, Felix von Oppen, and Matthew P. A. Fisher, Non-Abelian statistics and topological quantum information processing in 1D wire networks, *Nat. Phys.* **7**, 412 (2011).
- [20] Sandesh S. Kalantre, Justyna P. Zwolak, Stephen Ragole, Xingyao Wu, Neil M. Zimmerman, M. D. Stewart, and Jacob M. Taylor, Machine learning techniques for state recognition and auto-tuning in quantum dots, *npj Quantum Inf.* **5**, 6 (2019).
- [21] Justyna P. Zwolak, Sandesh S. Kalantre, Xingyao Wu, Stephen Ragole, and Jacob M. Taylor, QFlow lite dataset: A machine-learning approach to the charge states in quantum dot experiments, *PLoS One* **13**, 1 (2018).
- [22] Justyna P. Zwolak, Thomas McJunkin, Sandesh S. Kalantre, J. P. Dodson, E. R. MacQuarrie, D. E. Savage, M. G. Lagally, S. N. Coppersmith, Mark A. Eriksson, and Jacob M. Taylor, Auto-tuning of double dot devices in situ with machine learning (2019), arXiv:1909.08030.
- [23] Tim Botzem, Michael D. Shulman, Sandra Foletti, Shannon P. Harvey, Oliver E. Dial, Patrick Bethke, Pascal Cerdantaine, Robert P. G. McNeil, Diana Mahalu, Vladimir Umansky, Arne Ludwig, Andreas Wieck, Dieter Schuh, Dominique Bougeard, Amir Yacoby, and Hendrik Bluhm, Tuning Methods for Semiconductor Spin Qubits, *Phys. Rev. Appl.* **10**, 054026 (2018).
- [24] C. J. van Diepen, P. T. Eendebak, B. T. Buijtendorp, U. Mukhopadhyay, T. Fujita, C. Reichl, W. Wegscheider, and L. M. K. Vandersypen, Automated Tuning of Inter-Dot Tunnel Coupling in Double Quantum Dots, *Appl. Phys. Lett.* **113**, 033101 (2018).
- [25] Julian D. Teske, Simon Sebastian Humpohl, René Otten, Patrick Bethke, Pascal Cerdantaine, Jonas Dedden, Arne Ludwig, Andreas D. Wieck, and Jörg Hendrik Bluhm, A Machine Learning Approach for Automated Fine-Tuning of Semiconductor Spin Qubits, *Appl. Phys. Lett.* **114**, 133102 (2019).
- [26] N. M. van Esbroeck, D. T. Lennon, H. Moon, V. Nguyen, F. Vigneau, L. C. Camenzind, L. Yu, D. M. Zumbühl, G. A. D. Briggs, D. Sejdinovic, and N. Ares, Quantum device fine-tuning using unsupervised embedding learning (2020), arXiv:2001.04409.
- [27] A. R. Mills, M. M. Feldman, C. Monical, P. J. Lewis, K. W. Larson, A. M. Mounce, and J. R. Petta, Computer-Automated Tuning Procedures for Semiconductor Quantum Dot Arrays, *Appl. Phys. Lett.* **115**, 113501 (2019).
- [28] D. T. Lennon, H. Moon, L. C. Camenzind, Liuqi Yu, D. M. Zumbühl, G. A. D. Briggs, M. A. Osborne, E. A. Laird, and N. Ares, Efficiently measuring a quantum device using machine learning, *npj Quantum Inf.* **5**, 79 (2019).
- [29] H. Moon, D. T. Lennon, J. Kirkpatrick, N. M. van Esbroeck, L. C. Camenzind, Liuqi Yu, F. Vigneau, D. M. Zumbühl, G. A. D. Briggs, M. A. Osborne, D. Sejdinovic, E. A. Laird, and N. Ares, Machine learning enables completely automatic tuning of a quantum device faster than human experts (2020), arXiv:2001.02589.
- [30] T. A. Baart, P. T. Eendebak, C. Reichl, W. Wegscheider, and L. M. K. Vandersypen, Computer-Automated Tuning of Semiconductor Double Quantum Dots into the Single-Electron Regime, *Appl. Phys. Lett.* **108**, 213104 (2016).
- [31] Maxime Lapointe-Major, Olivier Germain, Julien Camirand Lemyre, Dany Lachance-Quirion, Sophie Rochette, Félix Camirand Lemyre, and Michel Pioro-Ladrière, Algorithm for automated tuning of a quantum dot into the single-electron regime (2019), arXiv:1911.11651.
- [32] Renato Durrer, Benedikt Kratochwil, Jonne V. Koski, Andreas J. Landig, Christian Reichl, Werner Wegscheider, Thomas Ihn, and Eliska Greplova, Automated tuning of double quantum dots into specific charge states using neural networks (2019), arXiv:1912.02777.
- [33] ‘QCoDeS: Python-based data acquisition framework,’ (2016), [Online; accessed October 2019].
- [34] W. G. van der Wiel, S. De Franceschi, J. M. Elzerman, T. Fujisawa, S. Tarucha, and L. P. Kouwenhoven, Electron

- transport through double quantum dots, *Rev. Mod. Phys.* **75**, 1 (2002).
- [35] Yaniv Taigman, Ming Yang, Marc'Aurelio Ranzato, and Lior Wolf, in *Proceedings of the IEEE Computer Society Conference on Computer Vision and Pattern Recognition* (IEEE Computer Society, 2014) pp. 1701–1708..
- [36] Alex Graves, and Navdeep Jaitly, in *Proceedings of the 31st International Conference on Machine Learning*, Proceedings of Machine Learning Research, Vol. 32, edited by Eric P. Xing and Tony Jebara (PMLR, Beijing, China, 2014), pp. 1764–1772.
- [37] Emmanuel Gbenga Dada, Joseph Stephen Bassi, Haruna Chiroma, Shafi'i Muhammad Abdulhamid, Adebayo Olu-sola Adetunmbi, and Opeyemi Emmanuel Ajibawa, Machine learning for email spam filtering: Review, approaches and open research problems, *Heliyon* **5**, e01802 (2019).
- [38] Giuseppe Carleo, and Matthias Troyer, Solving the quantum many-body problem with artificial neural networks, *Science* **355**, 602 (2017).
- [39] Giuseppe Carleo, Yusuke Nomura, and Masatoshi Imada, Constructing exact representations of quantum many-body systems with deep neural networks, *Nat. Commun.* **9**, 5322 (2018).
- [40] Giacomo Torlai, Guglielmo Mazzola, Juan Carrasquilla, Matthias Troyer, Roger Melko, and Giuseppe Carleo, Neural-network quantum state tomography, *Nat. Phys.* **14**, 447 (2018).
- [41] Hendrik Poulsen Nautrup, Nicolas Delfosse, Vedran Dunjko, Hans J. Briegel, and Nicolai Friis, Optimizing quantum error correction codes with reinforcement learning (2018), arXiv:1812.08451.
- [42] Ryan Sweke, Markus S. Kesselring, Evert P. L. van Nieuwenburg, and Jens Eisert, Reinforcement learning decoders for fault-tolerant quantum computation (2018), arXiv:1810.07207.
- [43] M. Ciorga, A. Sachrajda, P. Hawrylak, C. Gould, P. Zawadzki, S. Julian, Y. Feng, and Z. Wasilewski, Addition spectrum of a lateral dot from Coulomb and spin-blockade spectroscopy, *Phys. Rev. B* **61**, R16315 (2000).
- [44] X. G. Croot, S. J. Pauka, J. D. Watson, G. C. Gardner, S. Fallahi, M. J. Manfra, and D. J. Reilly, Device Architecture for Coupling Spin Qubits via an Intermediate Quantum State, *Phys. Rev. Appl.* **10**, 044058 (2018).
- [45] A. Ortiz-Conde, F. J. García Sánchez, J. J. Liou, A. Cerdeira, M. Estrada, and Y. Yue, A review of recent MOS-FET threshold voltage extraction methods, *Microelectron. Reliab.* **42**, 583 (2002).
- [46] Stéfan van der Walt, Johannes L. Schönberger, Juan Nunez-Iglesias, François Boulogne, Joshua D. Warner, Neil Yager, Emmanuelle Gouillart, Tony Yu, and The SciKit-Image Contributors, scikit-image: Image processing in Python, *PeerJ* **2**, e453 (2014).
- [47] F. Pedregosa, G. Varoquaux, A. Gramfort, V. Michel, B. Thirion, O. Grisel, M. Blondel, P. Prettenhofer, R. Weiss, V. Dubourg, J. Vanderplas, A. Passos, D. Cournapeau, M. Brucher, M. Perrot, and E. Duchesnay, Scikit-learn: Machine learning in Python, *J. Mach. Learn. Res.* **12**, 2825 (2011).
- [48] A. R. Mills, M. M. Feldman, C. Monical, P. J. Lewis, K. W. Larson, A. M. Mounce, and J. R. Petta, Computer-Automated Tuning Procedures for Semiconductor Quantum Dot Arrays, *Appl. Phys. Lett.* **115**, 113501 (2019).
- [49] J. M. Hornibrook, J. I. Colless, A. C. Mahoney, X. G. Croot, S. Blanvillain, H. Lu, A. C. Gossard, and D. J. Reilly, Frequency Multiplexing for Readout of Spin Qubits, *Appl. Phys. Lett.* **104**, 103108 (2014).
- [50] Robert E. Schapire, ‘A brief introduction to boosting,’ in *Proceedings of the 16th International Joint Conference on Artificial Intelligence - Volume 2*, series and number IJCAI’99 (Morgan Kaufmann Publishers Inc., San Francisco, CA, USA, 1999) pp. 1401–1406.
- [51] Christian Volk, Anasua Chatterjee, Fabio Ansaloni, Charles M. Marcus, and Ferdinand Kuemmeth, Fast charge sensing of Si/SiGe quantum dots via a high-frequency accumulation gate, *Nano Lett.* **19**, 5628 (2019).
- [52] E. Kawakami, P. Scarlino, D. R. Ward, F. R. Braakman, D. E. Savage, M. G. Lagally, Mark Friesen, S. N. Coppersmith, M. A. Eriksson, and L. M. K. Vandersypen, Electrical control of a long-lived spin qubit in a Si/SiGe quantum dot, *Nat. Nanotechnol.* **9**, 666 (2014).
- [53] A. R. Mills, D. M. Zajac, M. J. Gullans, F. J. Schupp, T. M. Hazard, and J. R. Petta, Shuttling a single charge across a one-dimensional array of silicon quantum dots, *Nat. Commun.* **10**, 1063 (2019).
- [54] Uditendu Mukhopadhyay, Juan Pablo Dehollain, Christian Reichl, Werner Wegscheider, and Lieven M. K. Vandersypen, A  $2 \times 2$  Quantum Dot Array with Controllable Inter-Dot Tunnel Couplings, *Appl. Phys. Lett.* **112**, 183505 (2018).
- [55] Torsten Karzig, Christina Knapp, Roman M. Lutchyn, Parsa Bonderson, Matthew B. Hastings, Chetan Nayak, Jason Alicea, Karsten Flensberg, Stephan Plugge, Yuval Oreg, Charles M. Marcus, and Michael H. Freedman, Scalable designs for quasiparticle-poisoning-protected topological quantum computation with majorana zero modes, *Phys. Rev. B* **95**, 235305 (2017).
- [56] S. M. Albrecht, A. P. Higginbotham, M. Madsen, F. Kuemmeth, T. S. Jespersen, J. Nygård, P. Krogstrup, and C. M. Marcus, Exponential protection of zero modes in Majorana islands, *Nature* **531**, 206 (2016).
- [57] V. Mourik, K. Zuo, S. M. Frolov, S. R. Plissard, E. P. A. M. Bakkers, and L. P. Kouwenhoven, Signatures of majorana fermions in hybrid superconductor-semiconductor nanowire devices, *Science* **336**, 1003 (2012).
- [58] Richard S Sutton, and Andrew G Barto, *Reinforcement Learning: An Introduction* (MIT press, London, England, 2018).
- [59] Jane Liu, and Mike West, in *Sequential Monte Carlo methods in practice* (Springer, 2001), pp. 197–223.
- [60] Christopher E Granade, Christopher Ferrie, Nathan Wiebe, and D. G. Cory, Robust online Hamiltonian learning, *New J. Phys.* **14**, 103013 (2012).